
Electronic Theses and Dissertations, 2020-

2023

Effect of Particle Size on Mechanics of Particle Reinforced Composites using Photoluminescence Piezospectroscopy

Khanh Vo
University of Central Florida

 Part of the [Mechanical Engineering Commons](#)

Find similar works at: <https://stars.library.ucf.edu/etd2020>

University of Central Florida Libraries <http://library.ucf.edu>

This Masters Thesis (Open Access) is brought to you for free and open access by STARS. It has been accepted for inclusion in Electronic Theses and Dissertations, 2020- by an authorized administrator of STARS. For more information, please contact STARS@ucf.edu.

STARS Citation

Vo, Khanh, "Effect of Particle Size on Mechanics of Particle Reinforced Composites using Photoluminescence Piezospectroscopy" (2023). *Electronic Theses and Dissertations, 2020-*. 1688.
<https://stars.library.ucf.edu/etd2020/1688>

EFFECT OF PARTICLE SIZE ON MECHANICS OF PARTICLE REINFORCED
COMPOSITES USING PHOTOLUMINESCENCE PIEZOSPECTROSCOPY

by

KHANH D. VO

B.S. University of Central Florida, Orlando, 2020

A thesis submitted in partial fulfillment of the requirements
for the degree of Master of Science
in the Department of Mechanical and Aerospace Engineering
in the College of Engineering and Computer Science
at the University of Central Florida
Orlando, Florida

Spring Term
2023

Major Professor: Seetha Raghavan

© 2023 Khanh D. Vo

ABSTRACT

Nanoparticle reinforced composites are greatly desired by the aerospace community for a multitude of applications for their tailorable quasi-isotropic mechanical properties such as the high strength-to-weight ratio. With increasing demand of structural nanoparticulate composites, the optimization of their structural integrity and performance can be improved with a better understanding of the load transfer mechanics. Extensive nanoparticulate composites research has focused on the roles of particle shape, size, and volume fraction on the mechanical properties. Nanocomposites are often experimentally characterized through the determination of the bulk composite material properties. Load transfer research with a micro-mechanics perspective, distinguishing particle and matrix behavior, has been explored significantly using analytical and finite element modeling. For a more complete understanding of load transfer mechanics of particle composites, high spatial resolution experiments measuring exclusively the particles strain response are valuable. In this work, photoluminescent piezospectroscopy (PLPS) uses the frequency shift of the stress sensitive R-lines to non-destructively establish the mechanics of 100 nm, 150 nm, and 350 nm Cr³⁺ doped -alumina nanoparticles in an EPON 826 matrix under applied compressive stress. The R-lines' stress sensitivity represented by the piezospectroscopic (PS) coefficient is used here to assess the particles' load transfer capability. The PS coefficients allow us to investigate the load transfer variation with three different nanoparticle sizes. As the particle size reduces from 350 to 100 nm, the

PS coefficients show that the particles experience 59% more stress indicating that the load transfer escalates with smaller particle sizes. This work also utilizes the R-line luminescent lifetime decay and assesses its reliability for stress measurements of particles within the composites. The lifetime decay measurements demonstrated significant inconsistencies due to the large variation in particle dispersion. The findings unravel the effect of particle size, to support new load transfer models that can be leveraged to tailor the design of structural nanocomposites.

To my dear loved ones, friends and family, that have supported me and my journey.

ACKNOWLEDGMENTS

I would like to acknowledge the many colleagues and collaborators that I've had the pleasure to work with in this project. I would like to thank my advisor Dr. Seetha Raghavan for her persistent support and guidance as a researcher in the Raghavan Research Group. Special thanks to Dr. Gou and the Boeing Corporation for their support in fabricating the specimens in this study. Special thanks to Dr. Ghosh as well for his invaluable assistance necessary to complete this work. Thanks to Amanda Stevenson and Dr. Frehofer, whose prior work has paved the way for my research. I would also like to thank my fellow colleagues and friends Quentin Fouliard, Johnathan Hernandez, Zac Stein, Remelisa Esteves, and Perla Latorre Suarez who have all been great sources of inspiration and provided invaluable support in the course of my research. This work was funded by the National Science Foundation under Grant No. IIP 1701983.

TABLE OF CONTENTS

LIST OF FIGURES	x
LIST OF TABLES	xiii
CHAPTER 1 : INTRODUCTION	1
1.1 Particle Reinforced Composites in the Aerospace industry	1
1.2 Effect of Reinforcements on Mechanical Properties	2
1.2.1 Volume Fraction Effect	3
1.2.2 Particle Size Effect	4
1.3 Motivation	6
1.4 Study Objectives	6
CHAPTER 2 : MECHANICS OF PARTICLE REINFORCED NANOCOMPOSITES ...	8
2.1 Load Transfer Mechanics Theories	8
2.1.1 Volume Fraction	10
2.1.2 Particle Size	12

2.2	Optical measurements for Composites	14
2.2.1	Theory of Piezospectroscopy using α -Alumina	14
2.2.2	Theory of Lifetime Decay	18
CHAPTER 3 : BULK ALUMINA COMPRESSION AND EXPERIMENTAL PARAME-		
TER DEFINITION AND SETUP		22
3.1	Study Objectives	22
3.2	Compression Calibrant Sample	23
3.3	Bulk Alumina Experimental Setup	25
3.4	Bulk Alumina Compression Calibration Results	28
3.4.1	Photoluminescent Peak Shift with Bulk Alumina Results	28
3.4.2	Digital Image Correlation with Bulk Alumina Results	29
3.4.3	Photoluminescent Lifetime Decay with Bulk Alumina Results	31
3.5	Fabrication of the 14Vf% nanocomposites with Different Particle Sizes	32
CHAPTER 4 : LOAD TRANSFER MECHANICS USING PHOTOLUMINESCENT SPEC-		
TROSCOPY		37
4.1	Study Objectives	37
4.2	Dispersion Mapping of Alumina Epoxy Nanocomposites	38
4.3	PS Coefficients of 14% VF Nanocomposites with Varying Particle Size	40

4.3.1	PS Coefficient for 100 nm 14% Volume Fraction Nanocomposites	41
4.3.2	PS Coefficient for 150 nm 14% Volume Fraction Nanocomposites	44
4.3.3	PS Coefficient for 350 nm 14% Volume Fraction Nanocomposites	46
4.4	Effect of Particle Size on Load Transfer	49
4.4.1	Luminescent Lifetime Coefficients for 14% VF with Varying Particle Sizes	52
4.4.2	DIC Results for 14% VF for Varying Particle Sizes	57
CHAPTER 5 : CONCLUSION		60
LIST OF REFERENCES		62

LIST OF FIGURES

Figure 2.1	Schematic of the piezospectroscopic theory explaining the spectral peakshifts due to stress	15
Figure 2.2	Theory of lifetime decay relating the a) energy level to the luminescence decay b) effects of temperature on lifetime c) change in lifetime due to compressive stress.	19
Figure 3.1	Measurement equipment setup and schematic	25
Figure 3.2	Rendered image of the alignment of the compression cuboid and depiction of the scanned regions within the region of interest	26
Figure 3.3	Peakshift trend of an Uniaxially loaded and a non-uniaxially alumina calibrant	28
Figure 3.4	Initial DIC of non uniform stress and signs of bending	30
Figure 3.5	Luminescent lifetime decay measurements of polycrystalline alumina in compression with an uneven stress distribution vs an even stress distribution as a result of experimental setup.	31
Figure 3.6	R-lines from 100, 150, and 350 nm particle size	34

Figure 3.7	Rendered image of the compression cuboid and depiction of the scanned regions within the region of interest (Green: PL mapping and point measurements) (Blue: Lifetime point measurement)	35
Figure 4.1	R1 intensity dispersion through the 14 VF% alumina epoxy samples	39
Figure 4.2	Applied stress free peak shift map with R-line fits for the 100 nm particle size 14% VF.	41
Figure 4.3	PL peak shift contours shown at discrete loads above for the 10 nm particle size 14%VF.	42
Figure 4.4	R1 PS coefficient of 100 nm particle size and 14% VF across 3 different samples.	42
Figure 4.5	R2 PS coefficient of 100 nm particle size and 14% VF across 3 different samples.	43
Figure 4.6	Applied stress free peak shift map with R-line fits for the 150 nm particle size 14% VF.	44
Figure 4.7	PL peak shift contours shown at discrete loads above for the 150 nm particle size 14%VF.	45
Figure 4.8	R1 PS coefficient of 150 nm particle size and 14% VF across 3 different samples	45
Figure 4.9	R2 PS coefficient of 150 nm particle size and 14% VF across 3 different samples.	46
Figure 4.10	Applied stress free peak shift map with R-line fits for the 350 nm particle size 14% VF.	47

Figure 4.11	PL peak shift contours shown at discrete loads above for the 350 nm particle size 14%VF.	47
Figure 4.12	PS coefficient of 350 nm particle size and 14% VF across 3 different samples	48
Figure 4.13	R2 PS coefficient of 350 nm particle size and 14% VF across 3 different samples.	48
Figure 4.14	Piezo-spectroscopic coefficient vs particle size	50
Figure 4.15	Tailoring of load transfer using particle size and volume fraction for alumina nanocomposites. The volume fraction effect on the load transfer is from Freihofer. [1]	52
Figure 4.16	Stress free time resolved normalized luminescence of 100 nm, 150 nm, and 350 nm particle sizes	53
Figure 4.17	Lifetime stress sensitivity of 350 nm particle size and 14 VF%	53
Figure 4.18	Lifetime stress sensitivity of 150 nm particle size and 14 VF%	54
Figure 4.19	Lifetime stress sensitivity of 350 nm particle size and 14 VF%	54
Figure 4.20	ϵ_{xx} and ϵ_{yy} maps at 10 MPa load increments of the 100 nm second sample. Non- uniaxial load becoming evident around the 100 MPa load step with the expansion of strain in the middle.	57

LIST OF TABLES

Table 3.1 Bulk alumina PS coefficients for R1 and R2 from literature [2]	24
Table 3.2 Prior lifetime in response to stress coefficients of both single crystal and polycrystalline alumina found in literature [3]	32
Table 4.1 R1 and R2 PS coefficients and stress ratios, defined by equation 4.1, for particle sizes 100, 150 and 350 nm.	50
Table 4.2 R-square of each sample and the averages for each particle size	51
Table 4.3 Lifetime stress sensitivity coefficients, $(a+\sigma b=\tau)$ and the stress ratios using the hydrostatic lifetime decay coefficient of 0.322 and 0.19 ms/GPa for low and high concentrations, respectively. [4, 5]	56
Table 4.4 Average elastic modulus of 14% VF with particle sizes of 100 nm, 150 nm, and 350 nm.	58

CHAPTER 1

INTRODUCTION

This chapter introduces the importance of particle reinforced nanocomposites for structural applications in the aerospace industry. The development of particle composites and its advantages is discussed. There is extensive research in the tailoring of particle composites concerning the volume fraction and particle size. The theories and models used today to predict the composites properties and explain the load transfer mechanics of the internal system is discussed. The reasoning for using photoluminescence piezospectroscopy to measure the load transfer and to assess the effects of particle size is addressed.

1.1 Particle Reinforced Composites in the Aerospace industry

Polymer nanocomposites have been a popular choice of material in the aerospace industry for more than 50 years as nanocomposites have brought great benefits with their high strength to weight ratio and unique properties. As the aerospace industry pushes for more cost efficient aircrafts through the development of new lightweight materials, particle nanocomposites have garnered increased interest. The usage of nanoparticles with various matrix materials boost significant fracture toughness and often elevates the mechanical, thermal, and electrical properties. These nanocomposites

often require relatively low dispersant and volume fraction to develop a homogeneously distributed composite with significant improvement in properties such as fracture toughness. [6, 7] Particle reinforced nanocomposites in the form of metal matrix composites are used in aircraft structures such as the landing gears, wings, and the engines. [8] Current day aircrafts, such as the Boeing 787 Dreamliner, can be composed up to 50% of composites, improving its fuel efficiency by 10% to 12%. [9] The further development of nanocomposites could allow for more ambitious light weight designs that could promote higher fuel efficiency. [10] To realize this potential, the design and tailoring of structural nanoparticle composites must be optimized through the understanding of the internal load transfer.

1.2 Effect of Reinforcements on Mechanical Properties

Substantial research has been conducted in the fine tuning and development of new composites. The composites mechanical performance can be enhanced by tailoring the components, volume fraction, shape, and size. Fiber composites are applied in a vast number of applications due to their high aspect ratio and anisotropic properties, allowing for improved load transfer between the matrix and reinforcements. [11] Short fibers are easier to handle, disperse, and are capable of conforming to complex shapes while providing a boost in mechanical properties. [12] The high surface area-to-volume ratio of nanoparticles allows for improved load transfer between the matrix and reinforcements with minimal volume fraction and dispersants. [13] With the increased surface area to volume ratio, a stronger interfacial bond can be created. The interphase is the concept

of a perturbed space around the particle that is defined by the interfacial bond. This concept is particularly useful as it may explain the mechanisms of the effective mechanical properties. [14] Nano-particles have also been used as secondary reinforcements in ternary composites, such as hybrid carbon fiber reinforced polymer composites, boosting mechanical properties such as their high strength and toughness. [15, 16, 17, 18, 19, 20, 21] The existence of the interphase and its properties can be determined through experimental means such as thermal analysis or atomic force spectroscopy. [22]

1.2.1 Volume Fraction Effect

The effect of the nanoparticles volume fraction has been extensively researched and often defined through the composites mechanical properties. The rule of mixtures dictates that with the increase of reinforcement volume fraction, mechanical properties such as the elastic modulus and strength would significantly improve. [23, 7, 24, 23] The wear loss in composites decreases with the increasing volume fraction and particle size. Diler notes that particle clustering can lead to increased wear loss beyond a certain volume fraction. [25] The effects of larger volume fractions on the composites properties can be attributed to the greater percolation. [26] The percolation increases as the average interparticle distance becomes smaller with higher volume fractions. [27, 28] As a result, the particles will have a larger influence on each other. [29, 30] Benefits such as the flexural modulus and toughness are seen to increase as particles get closer. [31]

Stress measurements were conducted by Stevenson and Freihofer using photoluminescence piezospectroscopy (PLPS) to study the load transfer of α -alumina nanoparticles in an epoxy matrix at 5%, 20%, 35%, 34%, and 38% VF. When the Cr^{3+} ion impurities in α -alumina are excited, the particles emit a stress sensitive spectral doublet band known as the R-lines. [32] The piezospectroscopic (PS) coefficients, Π , is the R-lines sensitivity to stress. The PS coefficients for the R1 and R2 peaks, were determined to be 7.59 and $7.62 \text{ cm}^{-1}/\text{GPa}$ for polycrystalline alumina, respectively. [33, 34] Using the PS coefficients obtained from the nanocomposites and the known bulk values, Stevenson and Freihofer determined the stress ratio of the particles for the different volume fractions. They found that with increasing volume fraction, the particles load transfer capability becomes greater as a function of the stress ratio. [35, 1] Freihofer adopted the same nanocomposite composition to develop a stress sensing coating for aerospace applications. [36, 37] Different volume fractions were experimented to determine the effectiveness of the particles load transfer to detect early failure in open hole tension composites. [38, 39, 40, 41]

1.2.2 Particle Size Effect

The smaller particle size has been linked to a number of improved properties and behaviors in materials. The increased surface area to volume ratio has been linked to stronger and more desirable properties in composites. The benefits of larger surface area to volume ratio has been attributed to Van der Waals forces. [42, 43, 44] The increased interfacial interactions enhances the adhesion strength and load transfer. [45] Cho researched the effect of the inclusion size from microns to

nanometers using both glass and alumina nanoparticles. His work attributed the improvement in the tensile strength, elastic modulus, and fracture toughness to the surface area to volume ratio. The adhesion strength greatly improved with smaller particles. [7] Though there is an increase in the elastic modulus, it is also consistent in literature that the particle size effect has a smaller impact than volume fraction. [46] The particle size effect is found to be more pronounced with larger volume fractions. [47] Gentieu found similar findings with the energy required to debond the particle using finite fracture mechanics and cohesive models. [48] Pinto demonstrated that small TiO₂ particle sizes of 17 and 50 nm at a low concentration yielded an improvement in the fracture toughness. The increase of fracture toughness should hold true as long as the particles are well dispersed. [49]

The effects of particle size in models are often represented with the application of the interphase. The application of the interphase could explain the differences in models and experimentally measured values. Jang's research demonstrated this in explaining the increase in young's modulus found in his experiments with micro and nano sized silicon dioxide. [50]. The interphase can be modeled to have the same properties as the matrix or vary along the length with different trends. [51, 52] Choi's research found that the interphase thickness should increase with the smaller particle sizes as the effective mechanical properties are dependent on its size. [53, 45, 54] With tools such as molecular dynamics, Marcadon found that the improvements were less restrictive with the interphase. While there is a substantial amount of research into the effects of particle size on the composite mechanical properties, there is a lack of studies aimed towards the measurement of load transfer distinguishing the particle and matrix contributions.

Some of the few experimental measurements regarding load transfer on a micro/nano scale that exist typically uses high resolution techniques. One such technique is raman spectroscopy which has been used to determine the load transfer for carbon nanotubes polymer composites. [55, 56, 57] Diffraction measurements has been employed in the measurement of particle residual stresses and load transfer. [58, 59, 60] The properties and size of the interphase of micro and nano sized particles have been experimentally measured through means such as atomic force spectroscopy and micro thermal analysis. [61, 62, 63, 22]

1.3 Motivation

To develop strong and tough nanocomposites, unique experimental measurements to quantify the effects of size on load transfer within the nanoparticles are needed. The potential for this work can be further extended to the validation of developing models and optimized design of new composites. To expand the field of particle stress measurements and assist in this effort, life-time decay stress measurements were also taken alongside photoluminescent piezospectroscopic measurements.

1.4 Study Objectives

To achieve the development of optimized structural particle nanocomposites, a set of objectives must be met. Firstly, the design and procedure for uniaxial compression procedure must be en-

sured. [64] To confirm uniaxial load, the obtained PS coefficient and the lifetime stress sensitivity using polycrystalline alumina must be validated with known published values. [34, 3] To establish the stress ratios to quantify the load transfer of the particles, the PS coefficients of the nanocomposites must be measured under uniaxial load. [35, 1]

CHAPTER 2

MECHANICS OF PARTICLE REINFORCED NANOCOMPOSITES

In this chapter the load transfer mechanics/theory of nanoparticle reinforced composites is discussed. Both effects of the particle size and volume fraction are reviewed. The second half of this chapter presents the theory behind both the photoluminescent piezospectroscopy and the lifetime decay used in this study.

2.1 Load Transfer Mechanics Theories

Several theories and models have been devised in the prediction and explanation of the composites material properties such as the elastic modulus. The rule of mixtures is a commonly used equation to predict the composites properties using the volume fractions and the material property of the phases in question. [65, 66]

The load transfer theories and models used to predict the composite properties and internal stresses are discussed. Eshelbys inclusion theory is used to express the load transfer from the peakshift results in the research done by Stevenson and Freihofer. [35, 1]

Eshelbys inclusion theory was devised to determine the elastic field of the inclusion and the matrix. [67, 68] To address the inhomogeneity problem, Eshelby devised a number of assumptions.

Some of these are (1) The inclusion is in an infinitesimal matrix. (2) Perfect bonding between the particle and matrix. (3) The particle is perfectly spherical. (4) Both are isotropic materials. With these assumptions, the classical theory could be used to determine remote stresses in the matrix, the elastic field of an inclusion, and all the stress and strain components at a point immediately outside the inclusion. The elastic field of the particle is a result of multiple acting strains as shown in equation 2.1.

$$\sigma^p = C^m(\epsilon^0 + \epsilon + \epsilon^*) \quad (2.1)$$

where σ^p is the stress of the particle, C is the stiffness tensor of the particle, ϵ^0 is the strain disturbed by the filler, ϵ is the mechanical strain from the matrix under applied load, and ϵ^* is the equivalent eigenstrain of the inclusion problem.

Theories have been developed extensively for reinforcements with large aspect ratios such as fibers. One prominent theory is the shear lag theory. The shear lag theory was developed by Cox to describe the distribution of stresses for long fibrous materials in composite materials, assuming that the load is carried primarily by the fiber parallel to it. [69] One of the significant aspects of this model is that the load is transferred through the shear stress onto the fiber. The stress at the ends of long fibers are expected to have non-uniform load at one end and low at the other end. As a result of the non uniform load transfer, the ends are typically neglected. Some other limitations of this theory are that it was designed for metal matrix composites and inaccurate for reinforcements with small aspect ratio and low volume fractions. [59, 70] Some of these reinforcements include short fibers and nanoparticles. The modified shear lag theory was developed by Nardone to adapt fillers with small aspect ratios, assuming that the fiber ends could not be ignored. [71]

The Mori-Tanaka method, which is based on Eshelbys' inclusion theory, is an effective mean field theory to predict the material properties, assuming isotropic and homogenous properties in the matrix. [72] It considers the volume fraction, the aspect ratio of the particles, and the properties of interest for the composite. [73] The method places a larger emphasis on multiple randomly placed and oriented particle interactions, and a uniform stress distribution in the matrix. [74] A similar effective mean field theory is the Halpin-Tsai method which is based on generalized self-consistent micromechanics. [75] The Halpin-Tsai method considers the same variables as the Mori-Tanaka but originally was intended for inclusions with larger aspect ratios such as unidirectional fibers. [73] Various studies have been attempted to expand the Halpin-Tsai method for randomly oriented inclusions and nanoparticles. [76, 77, 78] As effective mean field theories, the Mori-Tanaka and Halpin-Tsai method are more appropriate for assessing the materials performance rather than determining the particle stress itself.

2.1.1 Volume Fraction

It is commonly seen in most cases that with a greater amount of reinforcements there is a positive effect on the composite properties. This relationship between the reinforcement and epoxy is often predicted using the rule of mixtures as shown in equation 2.2. [65, 79, 66]

$$E_C = E_f V_f + E_m V_m \quad (2.2)$$

where E is the elastic modulus and V is the volume fraction. The subscripts c , f , and m represent the composite, filler, and matrix components in the composite, respectively. This form presented is the Voigt model and is often applied to any type of shape and the largest aspect of the reinforcement. The Reuss model would be the inverse to determine the transverse properties as shown in equation 2.3.

$$E_C = \left(\frac{V_f}{E_f} + \frac{V_m}{E_m} \right)^{-1} \quad (2.3)$$

The rule of mixtures is often used to predict the upper and lower bounds of the material properties with the Voigt and Reuss model, respectively. [79] For particle composites, the Voigt and Reuss models have also been identified with the iso-strain and iso-stress states, respectively. The iso-strain state is often associated with higher volume fractions as the higher number of particles have a greater influence on the load transferred. The iso-stress state is used for lower volume fractions as the matrix deformations are larger than the particles. [65] This method is limited in its accuracy and train of thought as factors such as particle size, interfacial bond, and distribution are known to have a large effect on composites performance. [80]

Percolation or the global geometrical connectivity in disordered systems also have a major role in the composites performance. [26] Percolation becomes a more prominent mechanism when the volume fraction surpasses the percolation threshold, or the critical volume fraction allowing for global connectivity among the inclusions. [81] The percolation of composites would lead to a significant boost in material properties with higher volume fractions compared to the linear rule of

mixtures. The sites or particles are connected through tunneling which can improve the transfer of load, electricity, and heat in the composite. [82, 81, 83]

The tunnel-percolation theory is regarded as a function of the interparticle distance. [27, 28] Higher volume fraction often is accompanied by the lower interparticle distances on average. [29] The interparticle distance is known to significantly increase the localized stress concentration in the matrix. [31] The increased clustering or agglomeration of particles will also elevate the localized stress concentration. [30]

As two particles make direct contact, hertzian contact dictates that the contact of the two particles may generate localized stress. [84] If there are dislocations or compaction in the particle, their surface defects that come into contact will turn into a interface dislocation allowing for the particles to relax. [85]

The percolation of a composite with excessive volume fraction can limit the interfacial area and exacerbate highly stressed regions. [86] This can reduce in the particle/matrix adhesion strength causing early failure. [87]

2.1.2 Particle Size

As the particle size decreases to nanometers, the adhesion strength and load transfer is found to have improved largely due the high specific surface area to volume ratio. [7] The larger specific surface area of the inclusions allows for greater interfacial region interaction and adhesion. [42, 88, 43] This is a result of the Van der Waals forces that act on the particle.

Van der Waals forces is the attraction between atoms and molecules defined in equation 2.4. As the nano-particulate reinforcements size continues to diminish, it is theorized that the Van der Waals forces become more prominent. [43, 80]

$$f_{vw}(r) = -\frac{AR_1R_2}{(R_1 + R_2)6r^2} \quad (2.4)$$

where R_1 and R_2 are the radius of the particles, A is the Hamaker constant, r is the distance between particles and f_{vw} is the Van der Waals force between particles. The Hamaker constant also becomes larger with dwindling particle size. [89] The increase Van der Waals forces with smaller particle enhances the attraction of particles and molecules resulting in worse dispersion and but also in greater adhesion with the matrix molecules. [42] When the particles are deformed under load, the total surface area of the particles will grow, leading to a greater Van der Waals force. [43]

Chen theorized that the interfacial adhesion strength as a function of the particle size can be characterized in equation 2.5. [44]

$$\sigma_0 = \sqrt{\frac{2AgE_p}{lG}} \quad (2.5)$$

where l is the particle size, E_p is the particle elastic modulus, g is the interface adhesion energy per unit area, A is the half area of the debonded interface, and G is a non-dimensional quantity. He goes further to theorize that a critical particle size exists in which no interface debonding would exist. [44] The improvement to the particle/matrix interfacial bonding allows for closer to perfect bonding for fuller load transfer to the inclusion.

The increased adhesion strength or interfacial bond will dictate the space around the particle creating the interphase. The interphase is commonly used in models to explain the differences in the modeled and experimental values. [45] It is generally agreed that the interphase region grows as the particle size gets smaller. [50] The property distribution of the interphase varies between studies as either a function of the power law or linearly. [90, 91] The increased surface area to volume ratio leads to a strong interfacial bond. The interphase properties and size is commonly thought to be the product of the interfacial bond. [92] This concept is particularly useful as it may explain the mechanisms of the effective mechanical properties. [14]

Another major influence to the load transfer of particles concerns the geometry itself. The stress flow interacting with the discontinuity that is the particle and other voids, produces a stress concentration. The decreased particle size results in a smaller curvature in the discontinuity. This tighter curvature produces a sharper stress concentration with more intense strain energy bounds of the inclusion leading to a higher elastic field. [93, 94, 95]

2.2 Optical measurements for Composites

2.2.1 Theory of Piezospectroscopy using α -Alumina

Photoluminescent piezospectroscopy provides a non-destructive measurement of the stress of Cr^{3+} doped alumina through the frequency shift of the R-lines. [32] One of the key characteristics of the R-line is the two stress sensitive peaks denoted as R1 and R2.

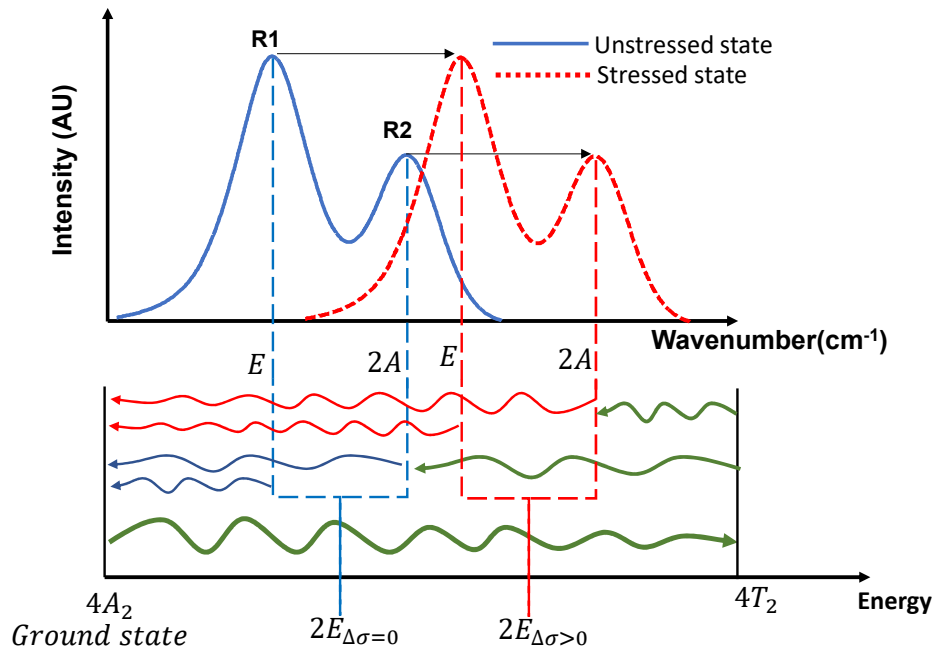


Figure 2.1: Schematic of the piezospectroscopic theory explaining the spectral peakshifts due to stress

This is seen when the chromium ions are distorted by the surrounding crystal field resulting in the split of the 2E energy level. [96] The valence electrons are excited to the 4T₂ shell using a 532 nm laser. Energy emitted from the electron returning to ground state interacts with the 2A and E shells producing the R1 and R2 doublet as shown in figure 2.1. [33] This doublet exhibits a lorentzian-gaussian blend characteristics. In its unstressed state, The R1 and R2 peaks are located around 14402 cm⁻¹ and 14432 cm⁻¹, respectively. With applied stress, the energy level emitted by the chromium ions changes resulting in the frequency shift. The R2 peak also exhibits a sensitivity to temperature and would broaden when under higher temperatures. The piezospectroscopic phenomona of these peaks can be related to stress using a tensorial relationship as shown in equation 2.6, as defined by Grabner. [32]

$$\Delta\nu = \Pi_{ij}\sigma_{ij} \quad (2.6)$$

Where $\Delta\nu$ is the peakshift, Π is the piezospectroscopic coefficient, and σ is the stress of the material.

Clarke further developed the PS equation for polycrystalline materials by inferring that the frequency shift would be the average of the crystallites over many and randomly oriented grains. This form of uniaxial stress is the average of the stresses and PS coefficients is shown in equation 2.7 and its simplified form in equation 2.8.

$$\Delta\nu = \frac{1}{3}(\Pi_{11} + \Pi_{22} + \Pi_{33})(\sigma_{11} + \sigma_{22} + \sigma_{33}) \quad (2.7)$$

$$\Delta\nu = \frac{1}{3}\Pi_{ii}\sigma_{ii} \quad (2.8)$$

For biaxial conditions, it would be 2/3rds and for hydrostatic conditions all the components would be considered. Photoluminescence piezospectroscopy continued to expand in its applications such as the assessment of the structural integrity of thermal barrier coatings (TBCs). [33, 97, 98, 99, 100] Clarke had measured the stress state and assessed the damage of TBCs by observing the R-lines from the thermally grown oxide, α -alumina (polycrystalline ruby), and its naturally occurring chromium ion impurities.

Through experimental means, He and Clarke determined the R1 and R2 PS coefficients of the three crystallographic directions for ruby shown in equation 2.9 and 2.10. [34]

$$\Delta\nu = \frac{1}{3}(2.56\sigma_{11} + 3.50\sigma_{22} + 1.53\sigma_{33}) \quad (2.9)$$

$$\Delta\nu = \frac{1}{3}(2.66\sigma_{11} + 2.80\sigma_{22} + 2.16\sigma_{33}) \quad (2.10)$$

The PS coefficient for poly crystalline alumina under hydrostatic stress for R1 is $7.59 \text{ cm}^{-1}/\text{GPa}$ and R2 is $7.62 \text{ cm}^{-1}/\text{GPa}$. For uniaxial stress, the R1 and R2 PS coefficient is approximately 2.53 and $2.54 \text{ cm}^{-1}/\text{GPa}$ for polycrystalline alumina, respectively.

In recent applications, polycrystalline alumina has been applied in multi-functional nanoparticulate form. [101, 102, 103, 39, 104, 105] Prior work with α -alumina epoxy nanocomposites, has been used in experiments to study the load transfer mechanics of particle composites in studies

such as volume fraction.[35, 106, 60] To define this load transfer, the following relationship for the nanocomposites was established in equation 2.11

$$\Delta v_{NC} = \Pi_{NC} \sigma_{applied} \quad (2.11)$$

where v_{NC} and Π_{NC} are the frequency shift and PS coefficient specific to the nanocomposite and $\sigma_{applied}$ is the stress applied to the nanocomposite. To reflect the load transfer ability of the particle itself in the nanocomposite. Freihofer and Stevenson related the bulk nature of the ceramic to the nanoparticle. [1, 35] This relationship is defined in equation 2.12. The stress ratio is represented in equation 2.13.

$$\Delta v_{NC} = \Pi_{NC} \sigma_{applied} = \Pi_{ii} \sigma_{ii} \quad (2.12)$$

$$\frac{\sigma_{ii}}{\sigma_{applied}} = \frac{\Pi_{NC}}{P_{ii}} \quad (2.13)$$

2.2.2 Theory of Lifetime Decay

The time resolved analysis of the spectral bands have often been used to also determine stress and temperature. [3, 4, 107, 108, 109, 110] The material specific radiative decay rate is often used to characterize the emission. The lifetime decay can be influenced by the defects in the particles. [111] The grain boundary and the dopant ions are typically classified as external defects. The

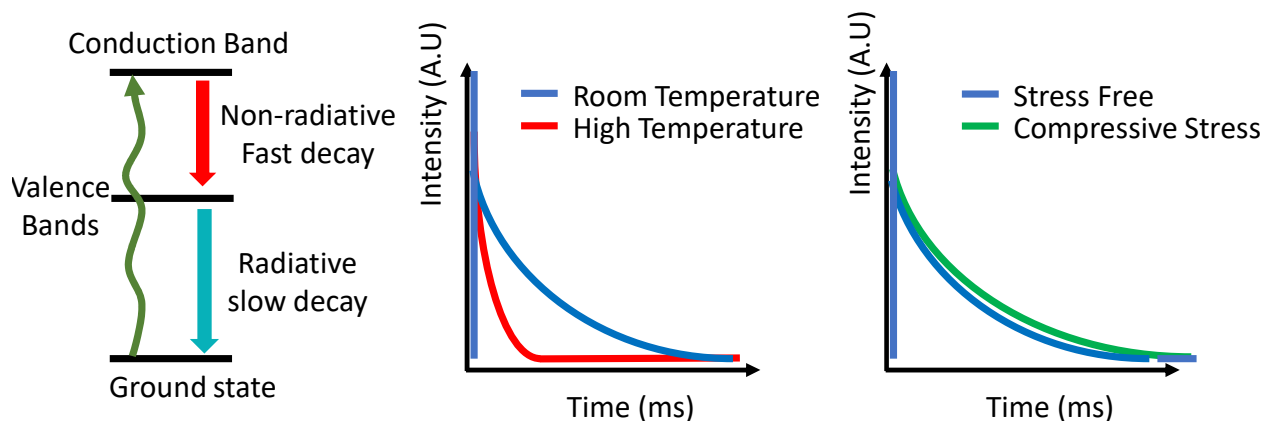


Figure 2.2: Theory of lifetime decay relating the a) energy level to the luminescence decay b) effects of temperature on lifetime c) change in lifetime due to compressive stress.

dopant concentration is a largely published factor in lifetime decay. [112, 113, 114] Anions and interstitial are classified as intrinsic defects. [115] When an electron is excited, it travels from the valence band to the conduction band. The photon emitted in a slow radiative decay as the electron travels towards the ground state for a vacancy in the valence bands. Defects or impurities such as the dopant atoms or vacancies can trap the electron reducing its mobility and thus its contribution to the radiative recombination. This trapping is known as quenching. [116] Trapped electrons are known to contribute in the non-radiative fast decay shown in figure 2.2. [111]

In Phosphor thermometry, the decay rate often decreases with higher temperature as shown in figure 2.2. [117, 107] One of the lesser used utilities of the lifetime decay is measuring stress.[96] This is more commonly seen in mechanoluminescent materials such as $SrAl_2O_4 : Eu^{2+}$. [118, 119]. The effects of pressure on ruby and aluminas lifetime decay has been thoroughly studied. [96] The lifetime decay increases as stress is applied as shown in figure 2.2. [4, 96]

The R1 luminescence lifetime decay of ruby under pressure was first studied by Sato-Sorensen and Merkle. [120, 4] The luminescent decay for the R-lines is best described as a stretched exponential as shown in equation 2.14. [96]

$$I(t) = I(0)e^{-(t/\tau_w)^{1/\gamma}} \quad (2.14)$$

Where I is the intensity of the signal, t is the time, τ_w is the mean lifetime decay, and γ is the stretch exponent. [96]

The relationship between the lifetime decay rate and stress can be expressed in a linear trend shown in equation 2.15.

$$\tau = a + bP \quad (2.15)$$

Where a is the stress free lifetime decay or τ_0 , the stress free decay rate, b is the lifetime variation with hydrostatic stress, and P is the stress applied to the material. Margueron and Clarke calculated τ_w value to approximately 0.307 ms/GPa with a chromium concentration below 0.3 a/o Cr. Table 3.2 is the experimentally determined lifetime with variation with under hydrostatic stress for single crystal and polycrystalline alumina recorded in literature. It should be noted that for uniaxial stress, the lifetime variation is expected to be one third as shown in equation 2.16.

$$\tau = a + \frac{1}{3}bP \quad (2.16)$$

Applying the same nanocomposite principles from frequency shifts to the lifetime stress sensitivity, the expected relationship between the inclusions lifetime and the nanocomposite lifetime is defined in equation 2.17.

$$\Delta\tau = \tau - \tau_0 = b_{ii}P_{ii} = b_{NC}P_{applied} \quad (2.17)$$

The particle size can be expected to have an effect on the lifetime decay as a result of the increased surface area. The exact effects on the lifetime measurement will depend on the defects and grain boundary. [121] If the grain boundary and defects are inconsequential of the increased surface area for smaller particles, the lifetime can be elongated. [122, 123] For alumina, increased trap sites are more available as a consequence. The effect on α -alumina lifetime decay is noted to be an increase in the fast exponential deviating from the normal stretch into a bi-exponential decay. [116] As the light emitted travels through the matrix from the alumina nanoparticles, the photons density of states is expected to reduce as a function of the effective composite refraction index thus impacting the lifetime decay. [124] Matrix materials with lower refractive index would allow for more light to be emitted from the system boosting lifetime decay. [124, 125] Local agglomerated regions may have a higher local refractive index and can result in a decrease in the radiative lifetime. [125]

CHAPTER 3

BULK ALUMINA COMPRESSION AND EXPERIMENTAL PARAMETER DEFINITION AND SETUP

In this chapter the details ensuing the preparation for the particle size studies using the alumina epoxy composite compression samples are discussed. A bulk alumina compression calibrant sample was tested and the compression testing procedure was devised in great detail in order to ensure the test setup would perform valid uniaxial load for the alumina epoxy samples that will follow in chapter 4. The basis of the compression calibrant sample design and its expected peak shift and lifetime trend are compared with known literature. [34, 96, 3] Issues that arose during the bulk alumina compression experiment are shown through the experimental results. Following that, the experimental equipment, setup, parameters and procedure were determined for the alumina epoxy samples and discussed in detail.

3.1 Study Objectives

To understand the load transfer mechanics of particle composites, the PS coefficient must be experimentally determined to quantitatively assess its load transfer capability. Before the alumina epoxy samples can be studied, a compression procedure for uniaxial load must be established. A

compression experiment was conducted to ensure uniaxial load through the validation of known PS coefficient and lifetime stress sensitive coefficient of bulk polycrystalline with prior literature. This validation ensures uniaxial load so that compression procedure can be used with confidence with the alumina epoxy experiments. [35, 126, 33, 3] Alumina epoxy nanocomposite compression samples were manufactured to experimentally determine the PS coefficient of different configurations and their relationships. Preliminary scans of the specimens were taken to optimize the collection parameters. The results of the alumina epoxy will also refer to previous studies for validation.

3.2 Compression Calibrant Sample

Polycrystalline alumina was chosen as the compression calibrant due to the amount of literature in which its PS coefficient has been defined as shown in table 3.1. Compression testing of high strength ceramics poses several challenges. The first is the ability to achieve uniaxial loading. Uniaxial load is essential in the compression testing of high strength ceramics. As ceramics have a high stiffness and are 10 to 15 times stronger in compression than in tension, tensile stresses stemming from non-uniaxial loads introduced by inaccuracies in the experimental setup will induce early failure. [64] Misalignment of the specimen in relation to the platens can introduce bending. Alignment tools were designed to ensure that the sample is concentric with the platens. Secondly, ceramics are hard to machine and this can result in non-parallel surfaces causing edge imperfections. When these imperfections are under load in the specimen/platen interface, bending and stress concentrations will arise and result in early failure and misleading low strength readings.

Thin copper sheets were used to fill in the gap in the interface to reduce the risks of stress concentrations and ensure even loading. Thirdly, the large difference in compliance or the mismatch of the material properties between the sample and the loading platen can lead to edge effects. The compliance factor for this experiment is considered for the elastic modulus, the hardness, friction, and the contact surface differences between the sample and the platen. This is addressed using intermediate sapphire platens with a larger surface contact area than the sample. This also introduces a medium for even distribution of stress. The shear stresses generated by the friction between the sapphire platens and the alumina is reduced by the application of a lubricant. The effects of these inaccuracies are shown and addressed in the experimentation of the compression sample through the validation of the polycrystalline alumina PS coefficient. The compression calibrant sample was made from a stock of alumina where a diamond saw was used to cut the material into a cuboid with the dimensions of 3.125 mm x 3.125 mm x 12.7 mm. [34, 33, 2]

Table 3.1: Bulk alumina PS coefficients for R1 and R2 from literature [2]

R1 (cm ⁻¹ /GPa)	R2 (cm ⁻¹ /GPa)	Source
2.6	2.63	Schawlow, 1961
2.6	2.5	Kaplyanskii & Przhhevuskii , 1962
2.4	2.3	Feher & Sturge, 1968
2.53	2.54	He & Clarke, 1995
2.46	2.5	Ma & Clarke, 1993
2.64	2.47	Raghavan & Imbrie, 2009

3.3 Bulk Alumina Experimental Setup

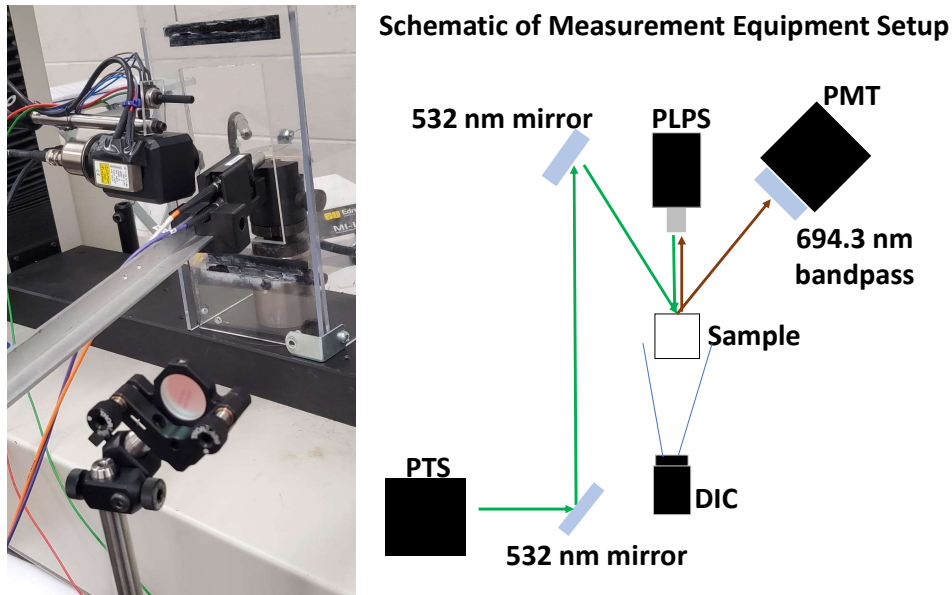


Figure 3.1: Measurement equipment setup and schematic

For this study, several means of measurements were devised to assess the stress/strain response of the polycrystalline alumina. Photoluminescent spectroscopic stress calibrations were determined through two methods of measurements, peak shift and lifetime decay. DIC was used to measure the bulk composite strain response and determine its mechanical properties. The schematic and the equipment is shown in figure 3.1. The peak shifts of the R-lines were measured using a photoluminescent portable spectroscopy system with a 532 nm continuous laser and a 694.3 nm bandpass to acquire the R-lines. [127]

A point measurement using PL with a collection of 30 points were used to assess its stress state for the PS coefficient determination. An exposure time and laser power of 30 ms and 2.5 mW were used. It should be noted that these particular PL collection parameters are specific to the

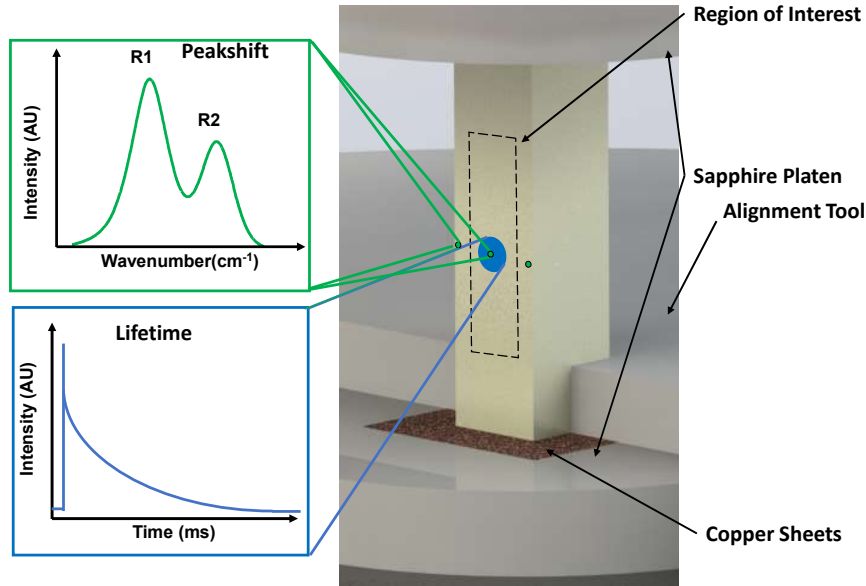


Figure 3.2: Rendered image of the alignment of the compression cuboid and depiction of the scanned regions within the region of interest

polycrystalline alumina experiment. At the start of each hold, a line scan is taken for on the spot analysis of both of the edges and the middle of the sample as shown in figure 3.2. [34] The edges are used to ensure uniaxial loading while the middle of the sample is used as the test section to validate that the R-lines are shifting as intended with the known PS coefficient.

To measure the lifetime decay, a 140 mW UV pulsed laser with a 532 nm crystal was used to excite the material. The signal was filtered through a 694.3 nm bandpass filter into a photo multiplier tube (PMT). [96, 3, 108] The signal was measured with a resistance of 10 k Ω , a gain of 27 mA, and a resolution of 500 mW and 2 ms. The pulsed laser excitation spot size is approximately 1 mm diameter as depicted in blue in figure 3.2. Using an oscilloscope connected to the PMT, 30 measurements were taken each hold, alternating with the PL measurements.

Digital Image Correlation was used as a secondary method to measure the strain of the material to confirm its mechanical properties and uniform loading. [128] The DIC images were collected at a rate of 1 frame per second while under load. The DIC camera is positioned facing the surface opposite to the surface where the spectral measurements are situated. Due to the DIC camera positioning directly behind the sample, precautions were taken to create a barrier to prevent the lasers from damaging the DIC camera CCD.

Compression force was applied onto the alumina epoxy samples with an MTS Insight with a 10 kN load cell. Initial measurements were taken starting at an initial stress of 100 MPa. Stress increments of approximately 50 MPa were implemented up to a max load of 900 MPa, at a crosshead displacement of 2 mm/minute as per ASTM standard C1424. [129] A hold of 3 minutes was imposed to allow for measurements to be collected and on spot analysis. Testing was halted when the material showed signs of plastic deformations or damage is discovered or when the on-spot analysis showed a drastic change in frequency shift trend.

Multiple compression trials with the polycrystalline alumina were conducted while optimizing uniaxial load for the experimental setup. 20 mm wide sapphire platens were used as an intermediary platen to address the effects of large compliance differences between the alumina and the metal platen and to prevent damage the metal platen. The load distribution is also addressed with the larger contact surface of the intermediate platen compared with the sample. A pair of alignment tools were designed to properly position the sample and sapphire platens into the middle of the steel platen and achieve a uniaxial load train. The alignment tools were kept in place up until there was sufficient load applied onto the sample preventing it from moving out of place. Copper

sheets with a thickness in the order of 0.1 mm were placed in the specimen/sapphire platen interface to fill gaps from any non parallelism and distribute the load. Lubricant was applied onto the sample surface and the sapphire platen to reduce the friction and therefore shear stresses. [64]

3.4 Bulk Alumina Compression Calibration Results

3.4.1 Photoluminescent Peak Shift with Bulk Alumina Results

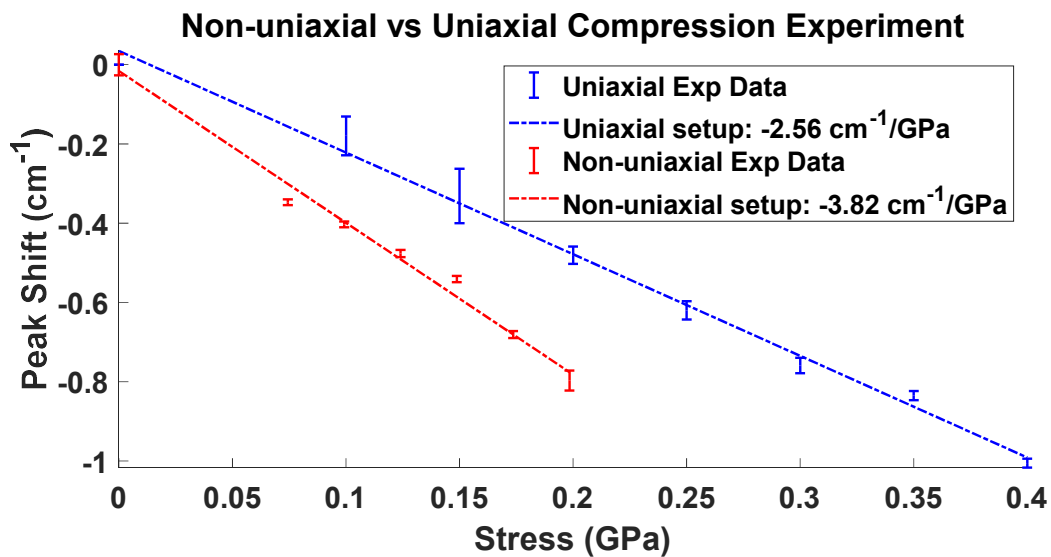


Figure 3.3: Peakshift trend of an Uniaxially loaded and a non-uniaxially alumina calibrant

In the experimentation of the bulk alumina, specific objectives were set to achieve the known PS coefficient with uniaxial loading and establish the experiment methodology and procedure. The initial challenges in this stemmed from non-uniaxial load transfer leading to increased non-

uniaxial loading. This was first evident in the determination of an incorrect PS coefficient of $3.82 \text{ cm}^{-1}/\text{GPa}$ as shown in figure 3.3. The PS coefficient indicates that non-uniaxial loading may have affected the experiment. This could be due to factors such as the non parallel features on the alumina surface in contact with the platen.

After the improvements to the compression experiment the peak shift data of the alumina calibrant yielded a PS coefficient that compared more favorably with that of published literature. The obtained PS coefficient, $2.56 \text{ cm}^{-1}/\text{GPa}$ from the improved experimental setup falls within bounds of the PS coefficients $2.4 - 2.64 \text{ cm}^{-1}/\text{GPa}$ from prior literature. [34, 34, 126]

3.4.2 Digital Image Correlation with Bulk Alumina Results

Uneven loading in the sample was identified using DIC measurement of the surface opposite from the laser probe. The DIC analysis, using NCORR, in figure 3.4, confirms a non-uniaxial state in the specimen. [130] This is shown throughout various load steps in figure 3.4. The e_{yy} demonstrates uniform strain up to 150 MPa. There is an increased magnitude of e_{xx} starting at 100 MPa indicating that the sample is bending. These patterns and behaviours were used as a basis for determining non-uniaxial loading for the composite samples.

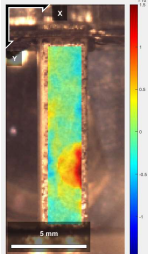
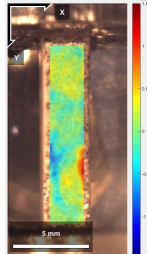
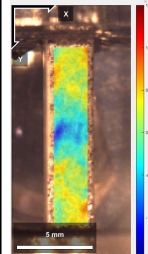
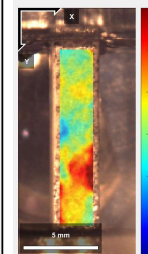
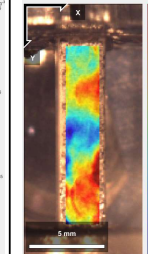
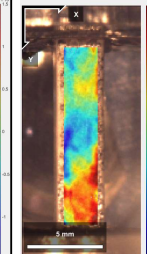
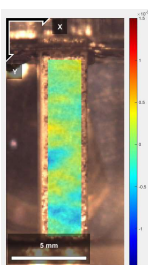
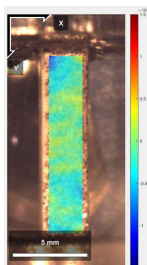
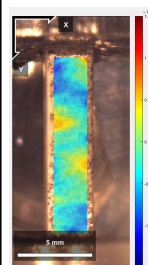
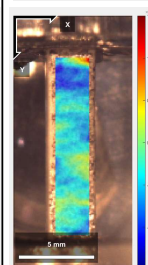
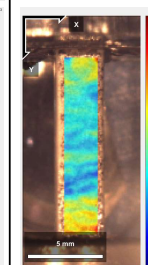
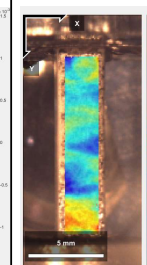
Load steps		3rd	4th	5th	6th	7th	8th
average σ_{yy} (MPa)	MTS Stress	27.73	53.66	78.06	100.76	128.76	153.26
	DIC Center	27.07303	22.35338	48.03344	72.39808	81.63669	79.23598
	DIC overall	31.74785	41.1811	70.22583	86.6702	71.28623	80.72263
Strain	ϵ_{xx}						
	ϵ_{yy}						

Figure 3.4: Initial DIC of non uniform stress and signs of bending

3.4.3 Photoluminescent Lifetime Decay with Bulk Alumina Results

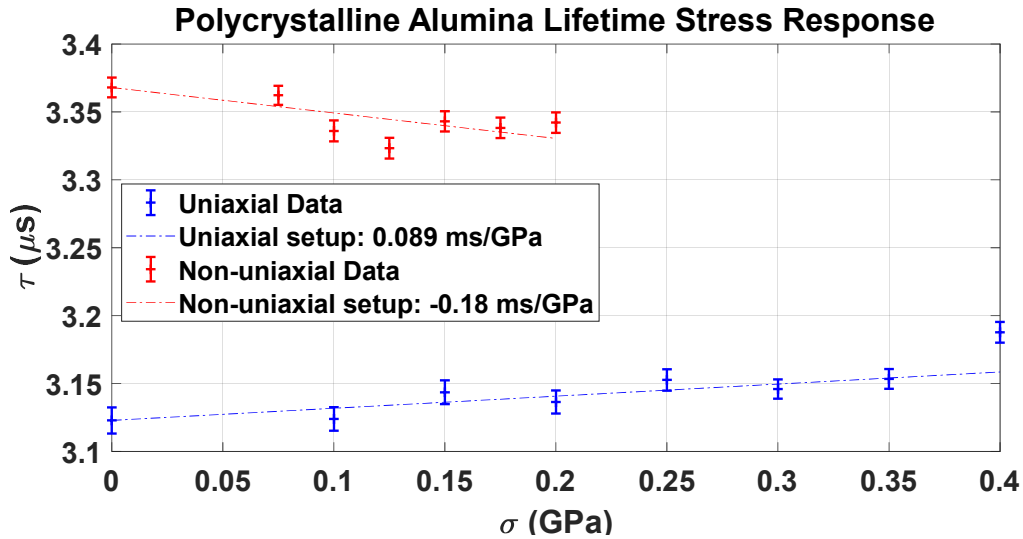


Figure 3.5: Luminescent lifetime decay measurements of polycrystalline alumina in compression with an uneven stress distribution vs an even stress distribution as a result of experimental setup.

The lifetime measurements shows a clear distinction between the uniaxially and non-uniaxially loaded alumina in its sensitivity to stress, b shown in table 3.2. For a uniaxial compression on α -alumina, the obtained b is expected to fall in the bounds of 0.063 - 0.102 ms/GPa based on prior literature in table 3.2. [3, 4, 5] The initial experiment has shown that the lifetime decay has shortened as seen in the negative slope. This is opposite from what is expected from literature as shown in figure 3.5. This shorter lifetime is thought to be the result of the larger excitation spot area that resulted in the non-uniaxial regions to be measured. The improved experimentation has yielded a lifetime stress sensitivity coefficient, 0.089 ms/GPa. which is well within the expected

Table 3.2: Prior lifetime in response to stress coefficients of both single crystal and polycrystalline alumina found in literature [3]

a (ms)	b (ms/GPa)	Crystal Structure	Cr ³⁺ Concentration	Source
3 ± 0.3	0.19 ± 0.07	Single Crystal	High Concentration	Merkle (1981)
2.6 ± 0.1	0.22 ± 0.01	Single Crystal	0.8%-1%	Sato-Sorensen (1986)
3.3 ± 0.5	0.245 ± 0.07	Single Crystal	0.5%	Eggert (1989)
3.04 ± 0.1	0.312 ± 0.02	Single Crystal	0.1%	Urocevic (1989)
3.5 ± 0.2	0.322 ± 0.03	Single Crystal	low	Jovanic (1990)
3.35	0.29	Single Crystal	0.3%	Margueron (2007)
2.27	0.307	Polycrystalline	0.3%	Margueron (2007)

bounds of prior literature. With the support of the more favorable b and Π values, the improved experimental compression procedure was deemed appropriate for the nanocomposite samples.

3.5 Fabrication of the 14Vf% nanocomposites with Different Particle Sizes

A total of 18 nanocomposite samples consisting of 100 nm, 150 nm and 350 nm particle sizes with 14% volume fraction were manufactured. 6 specimens were manufactured for each particle size. The 150 nm particle size was extensively studied in previous studies on the effects of volume fraction. [35] Alumina nanoparticles were procured from the same manufacturer, Advanced materials. The purity is about 99.99% for 100 nm and 98.85% for the larger particle sizes. The

epoxy resin and curing agent is epon 862 and Epikure W procured from Hexion. The manufacturing of the nanocomposite samples are based on prior work and literature. [131, 132, 133, 134, 35] Acetone was used to disperse the nanoparticles by using a sonicator for 30 minutes. The alumina nanoparticles were filtered out and dried out in the air after sonication. A thinky mixer was used to homogeneously disperse the resin, curing agent, and the nanoparticles with the desired volume fraction and particle size. The product is placed into a sonicator for 20 minutes to remove any air bubbles and for further homogenization. A low pressure desiccator-vacuum system was used for about 45 minutes or until no air bubbles were visible. Partall Hi-Temp Wax was used as a mold release for the mix and mold. A two step curing process of 6 hours at 54°C and 16 hours at 93°C. The specimens were cut using a diamond saw from the mold to the identical dimensions of the polycrystalline alumina compression specimen. Micron sized particles were also intended to be studied as well but issues with sedimentation for these sizes yielded poor quality specimens.

With the proven uniaxial compression procedure for the nanocomposites, the nanocomposites collection parameters must be optimized before the load transfer experiments. The specimens R-lines were measured to assess the signal quality of each particle size and determine the optimal collection parameters in figure 3.6. The intensity of the R-lines improves with larger particle sizes. It should be noted that the 350 nm shows the distinctly higher intensity than the smaller particles. The 100 nm and 150 nm particle size specimens indicate similar intensities. These R-lines were collected with a laser power of 30 mW. An exposure time of 30 ms with an average of 8 exposures per frame was used to obtain an optimal signal quality across all the samples.

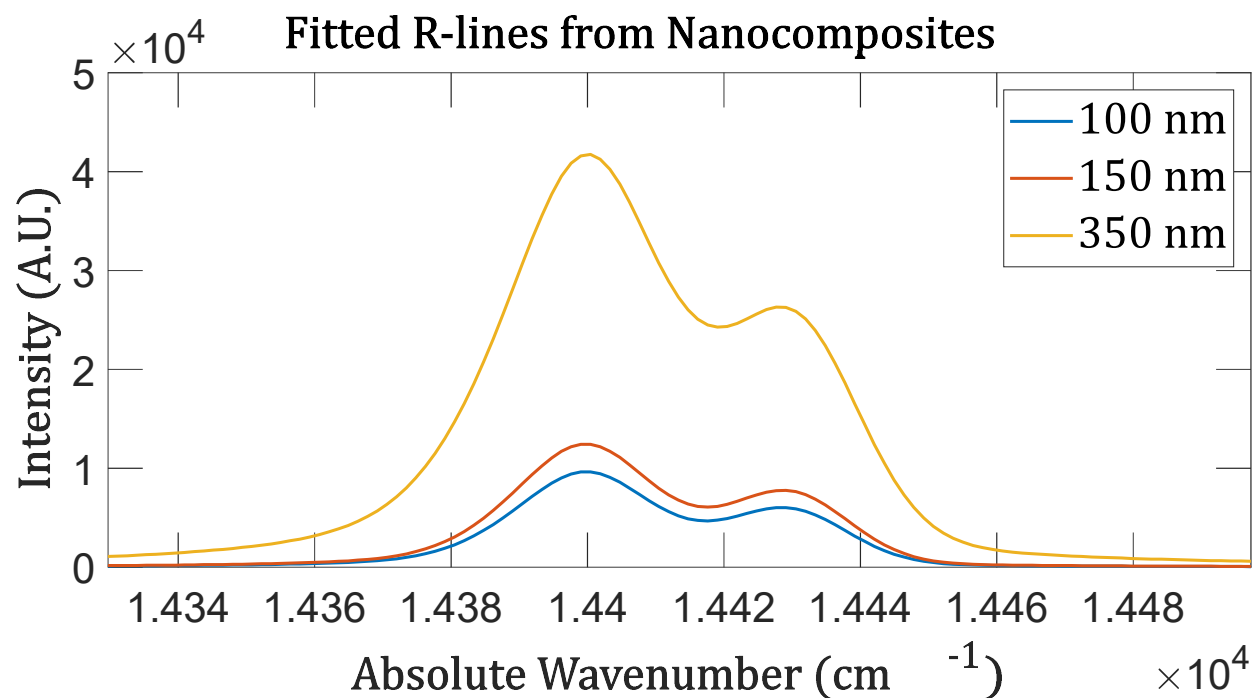


Figure 3.6: R-lines from 100, 150, and 350 nm particle size

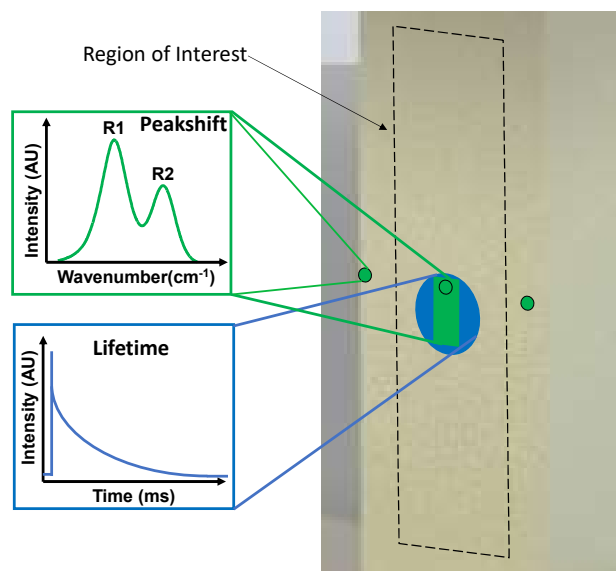


Figure 3.7: Rendered image of the compression cuboid and depiction of the scanned regions within the region of interest (Green: PL mapping and point measurements) (Blue: Lifetime point measurement)

The spatial variation of the nanoparticles requires the measurement of a wider area to determine the composite stress response. The alumina epoxy samples is scanned using an XYZ stage over an area of 0.5 mm x 1 mm with a spatial resolution of 0.1 mm in a snake scan pattern for a total of 50 points per hold as shown in figure 3.7. Compression force is applied onto the 14VF% alumina epoxy samples with an MTS Insight with a 5 kN load cell. With the rule of mixtures, the expected strength of the composites is approximately 0.11 GPa. Initial spectral measurements were taken starting at the zero load state. The samples were preloaded up to 0.01 GPa. The hold for spectral measurements started at 0.05 GPa. Stress increments of 5 MPa were implemented up to a max stress of 0.11 GPa. A crosshead displacement of 2 mm/minute as per ASTM standard E695. [135] A hold of 3 minutes was imposed to allow for measurements to be collected. The experiment and measurements halted when the on-spot analysis showed a drastic change in the PS coefficient indicating potential signs of plastic deformation.

Lifetime measurement parameters were also optimized for the nanocomposites. The luminescence of the R-lines indicated parameters with lower time resolution and sensitivity were needed. The laser power is consistent. The PMT measurements was improved with a resistance and gain of 50 k Ω and 37 mA, respectively. A resolution of 500 mW and 2 ms were used in the oscilloscope.

CHAPTER 4

LOAD TRANSFER MECHANICS USING PHOTOLUMINESCENT SPECTROSCOPY

In this chapter the effects of particle size on the load transfer mechanics was measured using photoluminescent piezospectroscopy. The nanocomposite manufacturing process and the particle dispersion was discussed and assessed. Experimental parameters were devised for higher sensitivity to measure the stresses more accurately. The PS coefficients of the R-lines was integral in the study of particle sizes. DIC was used to determine if the samples were under uniaxial load and their mechanical properties. Lifetime decay of the same R-lines was used to provide an additional measurement of particle stresses.

4.1 Study Objectives

The dispersion of the nanoparticles are assessed for uniform dispersion to determine the specimens best suited for compression testing. The measured R1 and R2 PS coefficients were used to quantify the increased load transfer with smaller particle sizes. The PS coefficients were characterized the load transfer through the stress ratio. The effect of particle size on the elastic modulus and yield

stress was determined using DIC. The lifetime decay measurements are assessed in its reliability to measure the particle stresses through the comparison of stress ratios from the peak shift results.

4.2 Dispersion Mapping of Alumina Epoxy Nanocomposites

The fabricated alumina epoxy nanocomposites particle dispersion needed to be assessed. Agglomerations or voids of particles can affect the stress distribution of the composite. [136] The R1 intensity was scanned from the entire surface to determine if the particle dispersion and signal quality is sufficient for experimentation. Particle agglomerations are expected to have greater luminescent intensity. Regions where particles are thinly spread out are expected to have lower intensities. The distribution of intensities is represented in a histogram plot as seen in figure 4.1. The histogram characteristics can be used to quantify and assess the characteristics and quality of the alumina nanoparticles dispersion. [137, 138, 139]

In figure 4.1, high and narrow peaks indicate that most of the particles have similar intensity across the region of interest. Wider and shorter peaks indicate that the particle distribution varies greatly. The position of the highest peak show that most of the sample region of interest has good quality signal for the R-lines with high intensity and SNR. Peaks further right and left of the highest peak may also help indicate the presence of agglomerations or thin regions, respectively. From figure 4.1, the 150 nm series shows the best dispersion of particles within a tight range of intensities compared to some of the other particle sizes, but some agglomerations are present within the structure of the sample. The 100 nm series shows that the dispersion quality among the

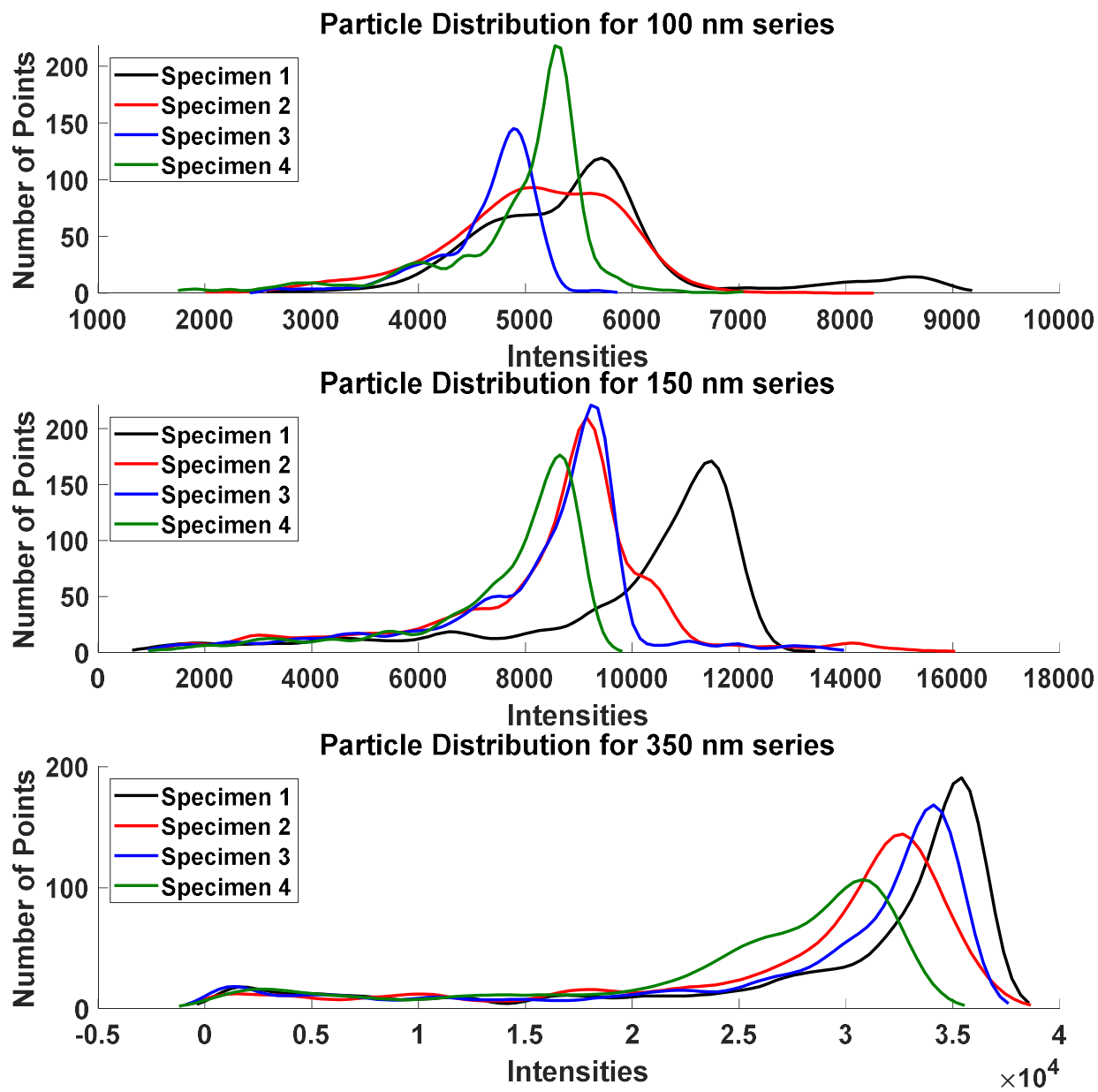


Figure 4.1: R1 intensity dispersion through the 14 VF% alumina epoxy samples

samples differs more than other two sets. These samples are expected to have the low signal quality and greater agglomeration than the 150 nm series. The 350 nm particle series has the best signal quality. However, the wider peaks also means that the dispersion of particles may vary more than the 100 and 150 nm. This is different from the expected trend as greater particle sizes should allow for greater dispersion than the smaller particle sizes. This can be attributed to the sedimentation of the 350 nm. The sedimentation for the 350 nm is not as severe compared the micron sized particles as discussed in the fabrication section but still has a significant effect on the particle distribution.

4.3 PS Coefficients of 14% VF Nanocomposites with Varying Particle Size

In this section, the stress state of the nanocomposites with 100, 150 and 350 nm particle sizes are discussed using PL spectroscopy with both peak shift and lifetime decay. DIC is used to measure the strain of the composite sample to determine the materials elastic modulus and the yield strength if reached. The 14% VF nanocomposites were all compressively loaded until the peak shift analysis showed signs of plastic deformation. The data in this discussion is only presented up to the end of the elastic region. The R-lines are observed to have a continuous peak shift until 80 to 95 MPa for all particle sizes. Each particle size set was tested with 3 different samples to determine an averaged piezospectroscopic coefficient.

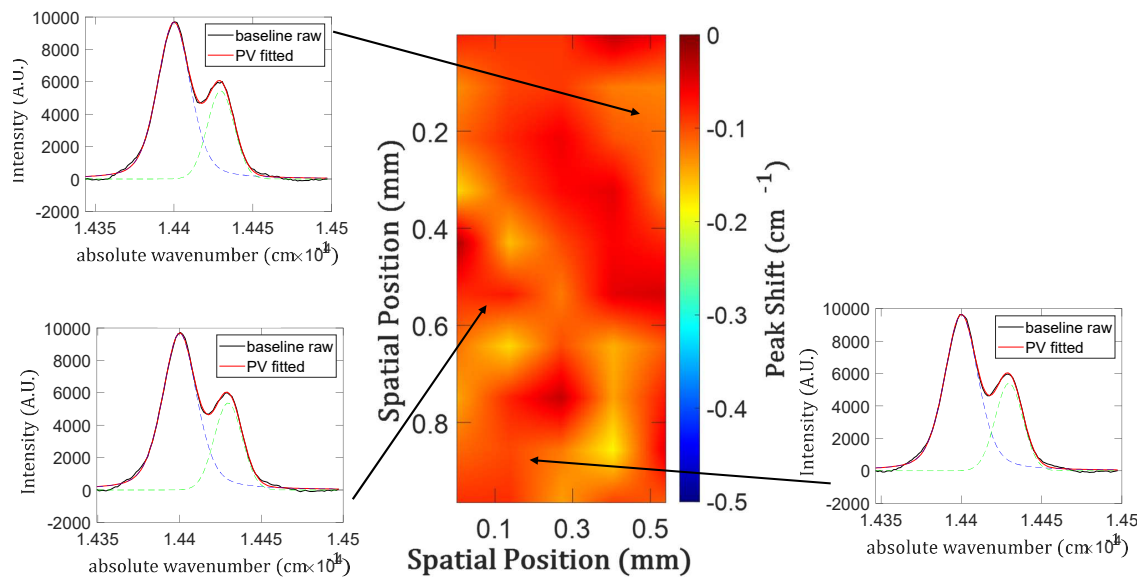


Figure 4.2: Applied stress free peak shift map with R-line fits for the 100 nm particle size 14% VF.

4.3.1 PS Coefficient for 100 nm 14% Volume Fraction Nanocomposites

The R1 and R2 peaks from the map scans from the 100 nm set are shown to fit properly in figure 4.2. The same fitting parameters were applied for all loads measured. Figure 4.3 contains the peak shift maps of the 100 nm particle size with applied uniaxial compression.

The R1 and R2 peak shift response to the applied compressive stress for 100 nm with 3 samples each are shown in figures 4.4 and 4.5. The R1 and R2 PS coefficients of each sample are shown in figures 4.4 and 4.5. The R1 and R2 PS coefficient obtained are $4.11 \text{ cm}^{-1}/\text{GPa}$ and $1.54 \text{ cm}^{-1}/\text{GPa}$, respectively. The error bars shown in these figures are based on the standard deviation of the peak shifts for each individual loads. The peak shift maps collected are shown in figure 4.3.

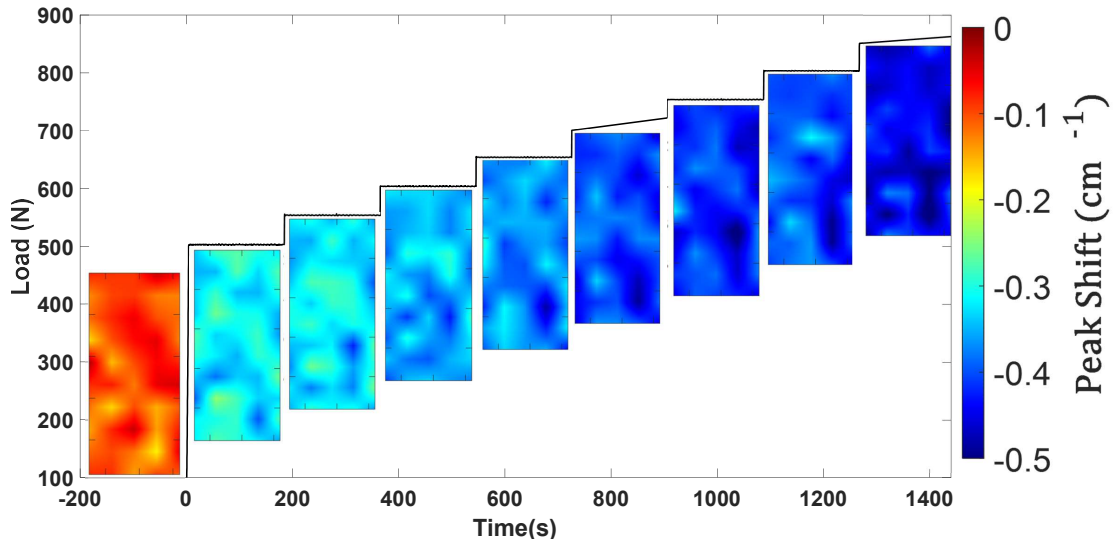


Figure 4.3: PL peak shift contours shown at discrete loads above for the 10 nm particle size 14%VF.

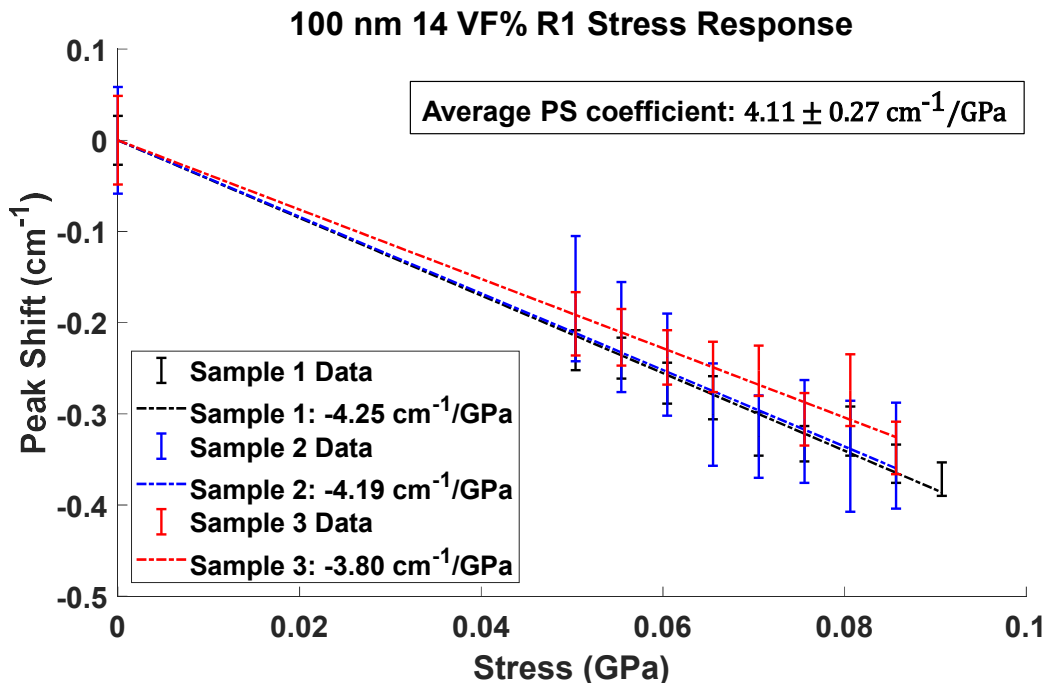


Figure 4.4: R1 PS coefficient of 100 nm particle size and 14% VF across 3 different samples.

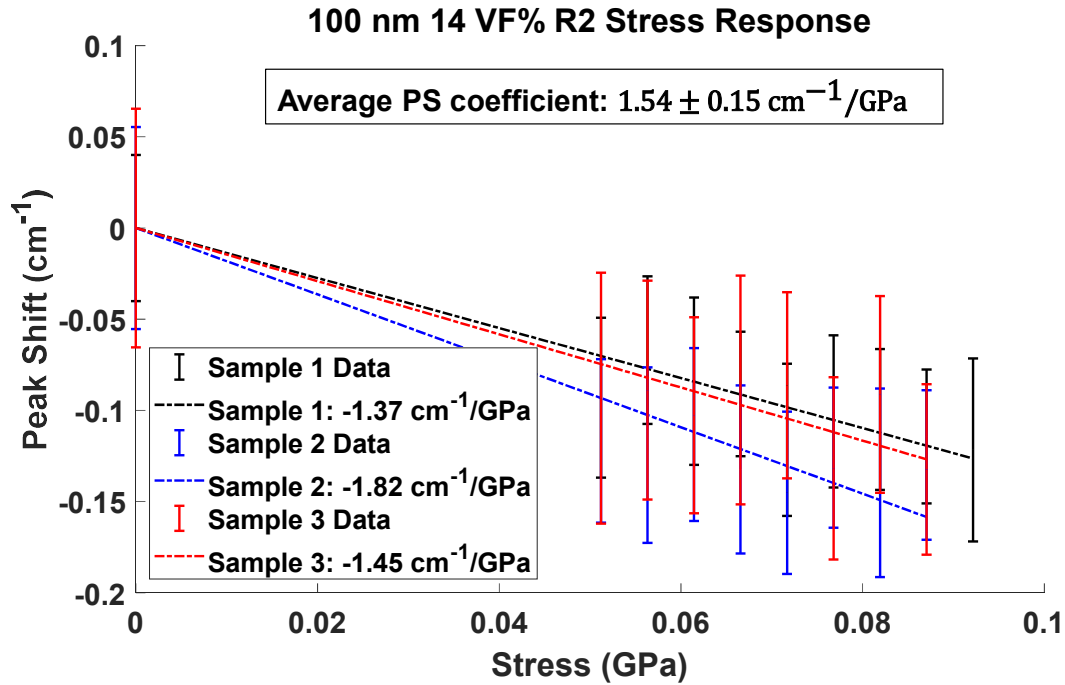


Figure 4.5: R2 PS coefficient of 100 nm particle size and 14% VF across 3 different samples.

It should be noted that for the 100 nm series the 2nd specimen shifted changing the region of interest when loaded. Points closest to the new region of interest were chosen as the zero load state. The three 100 nm samples are in good agreement with each other for the range of peak shifts measured. The R2 PS coefficients for the 100 nm particle size is lower compared to prior work with alumina nanocomposites. [35] This is likely due to the low SNR of the R2 peak for 100 nm series.

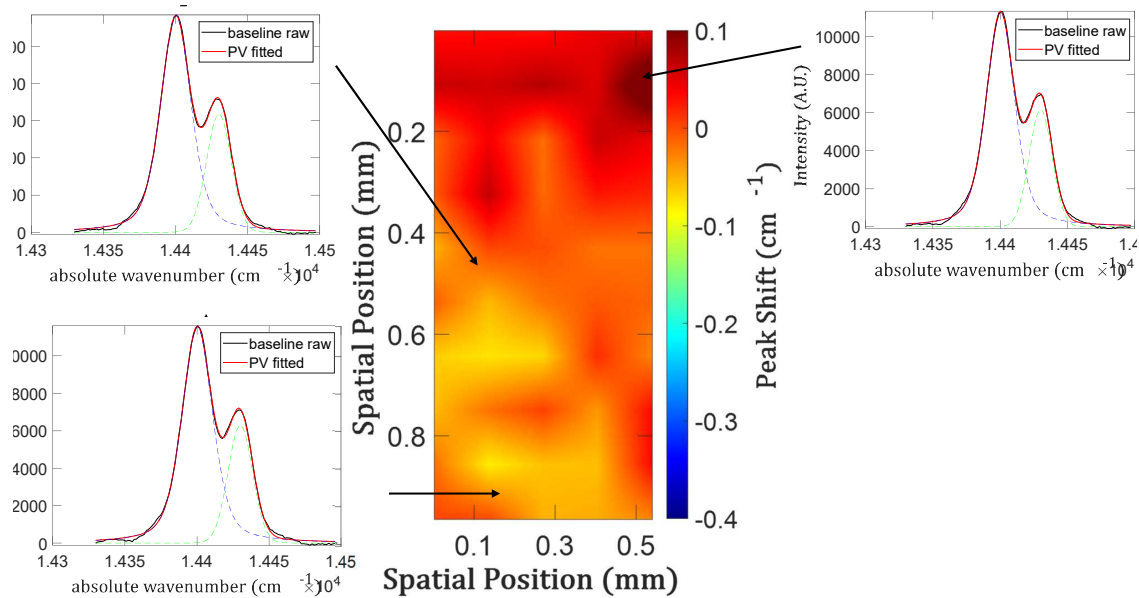


Figure 4.6: Applied stress free peak shift map with R-line fits for the 150 nm particle size 14% VF.

4.3.2 PS Coefficient for 150 nm 14% Volume Fraction Nanocomposites

The various residual peak shifts in the zero load map are shown to properly fit using the Pseudo-Voigt fit in figure 4.6. Throughout the experiment, a consistent peak shift concentration is observed in the top half of the region of interest in figure 4.7.

For the 150 nm series, the results for the 3 samples are in good agreement of each other for the range of peak shifts measured as shown in figure 4.8. This was especially true for later load steps past 700 N. The average R1 PS coefficient measured is approximately $3.18 \text{ cm}^{-1}/\text{GPa}$. In comparison to Stevensons results with 150 nm particle size, this PS coefficient at 14% VF falls within the bounds of 3.16 and $3.65 \text{ cm}^{-1}/\text{GPa}$, at 5% and 25% VF respectively. [35] The average

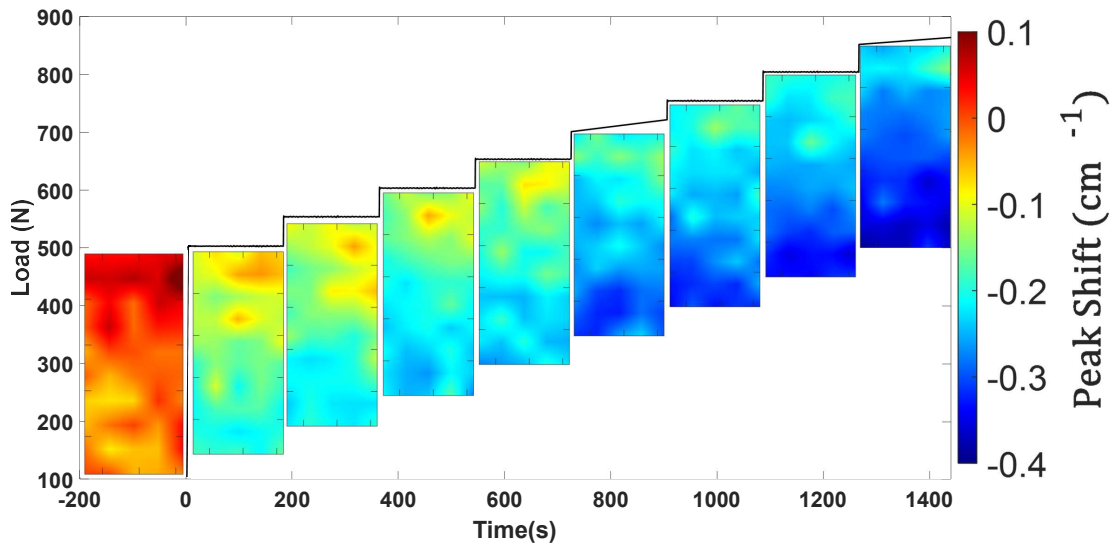


Figure 4.7: PL peak shift contours shown at discrete loads above for the 150 nm particle size 14% VF.

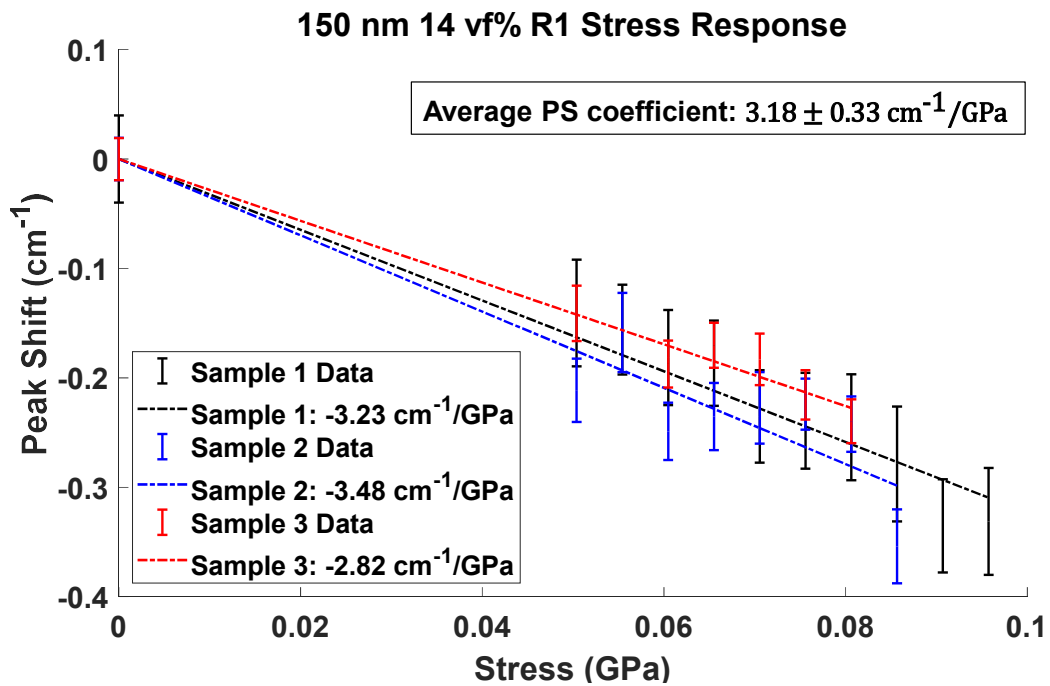


Figure 4.8: R1 PS coefficient of 150 nm particle size and 14% VF across 3 different samples

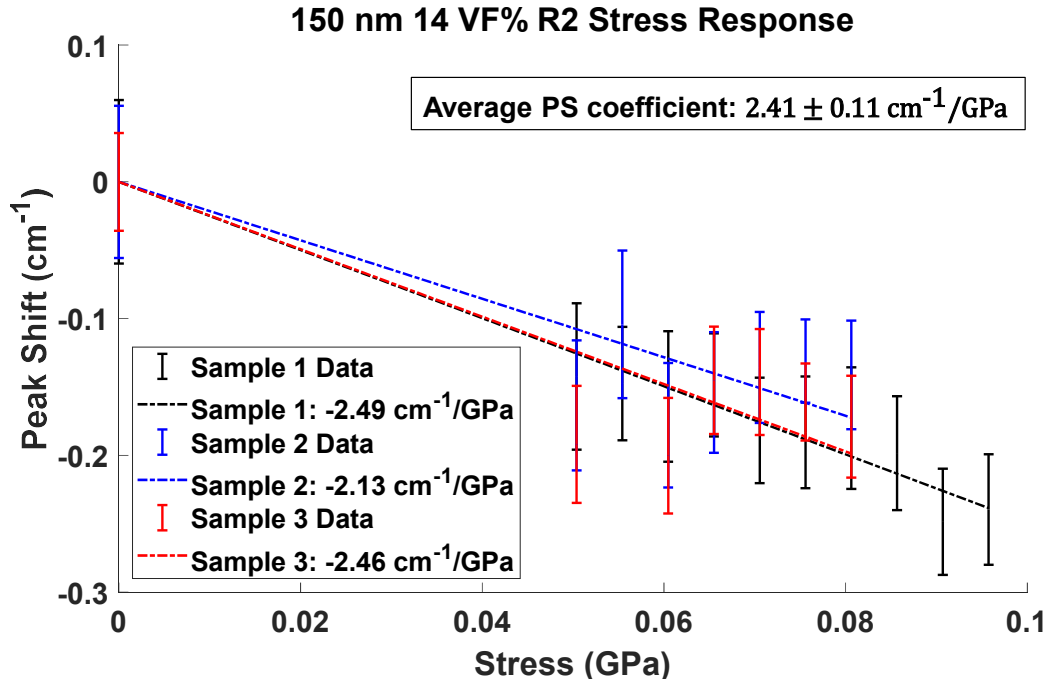


Figure 4.9: R2 PS coefficient of 150 nm particle size and 14% VF across 3 different samples.

R2 PS coefficient over the three specimens is $2.41 \text{ cm}^{-1}/\text{GPa}$ which is higher than the 100 nm particle size.

4.3.3 PS Coefficient for 350 nm 14% Volume Fraction Nanocomposites

The various residual peak shifts in the zero load map are shown to properly fit using the Pseudo-Voigt fit in figure 4.6. Through out the experiment, a consistent peak shift concentration is observed in the top half of the region of interest in figure 4.7.

The sample quality of the 350 nm indicate a gradient of residual peak shifts, in figure 4.10. The 350 nm series R1 data perhaps has the highest variation in peak shifts over different compressive

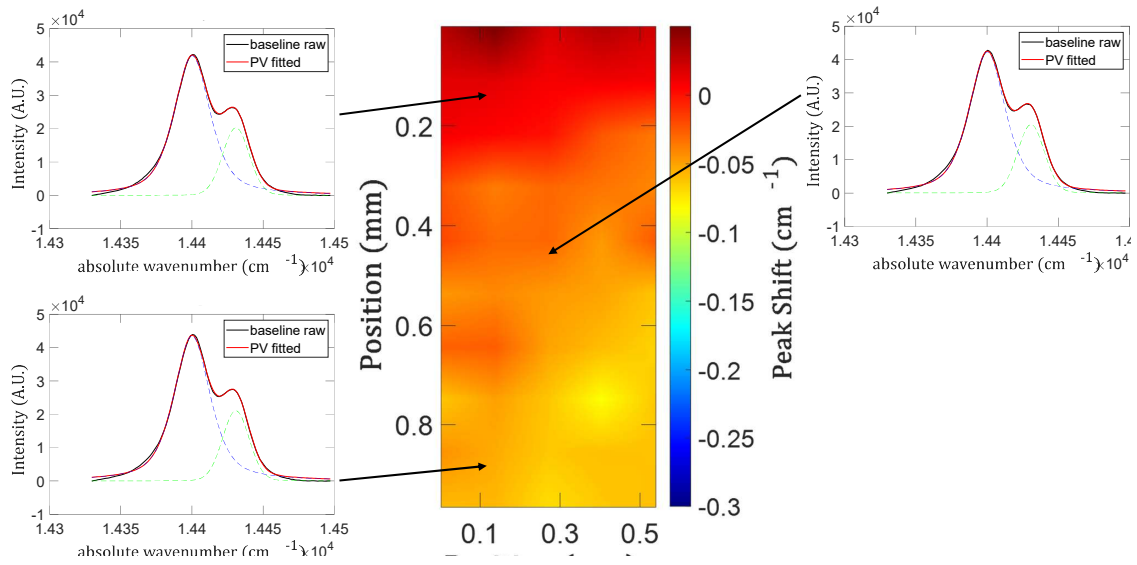


Figure 4.10: Applied stress free peak shift map with R-line fits for the 350 nm particle size 14%

VF.

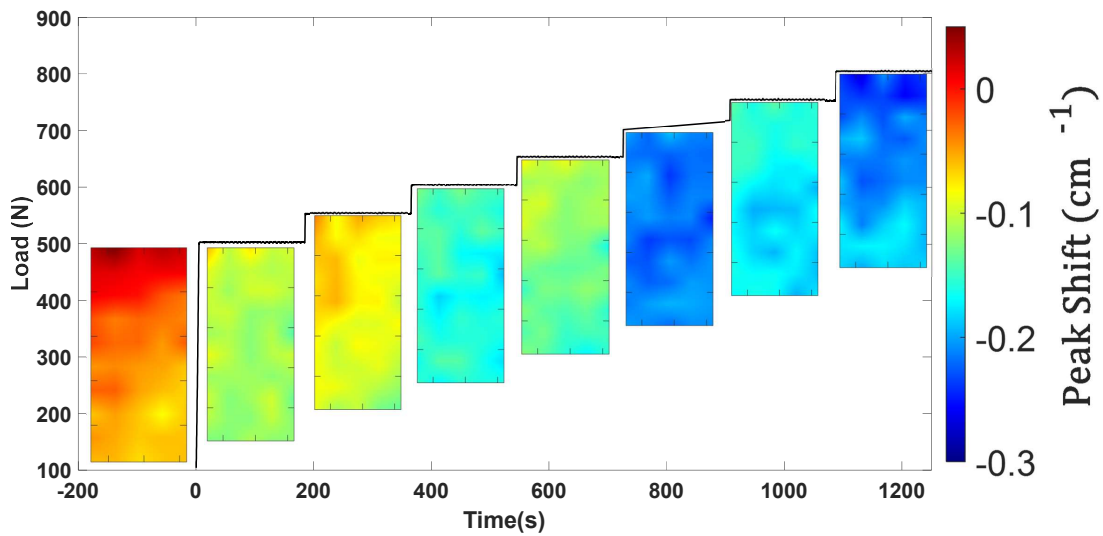


Figure 4.11: PL peak shift contours shown at discrete loads above for the 350 nm particle size

14% VF.

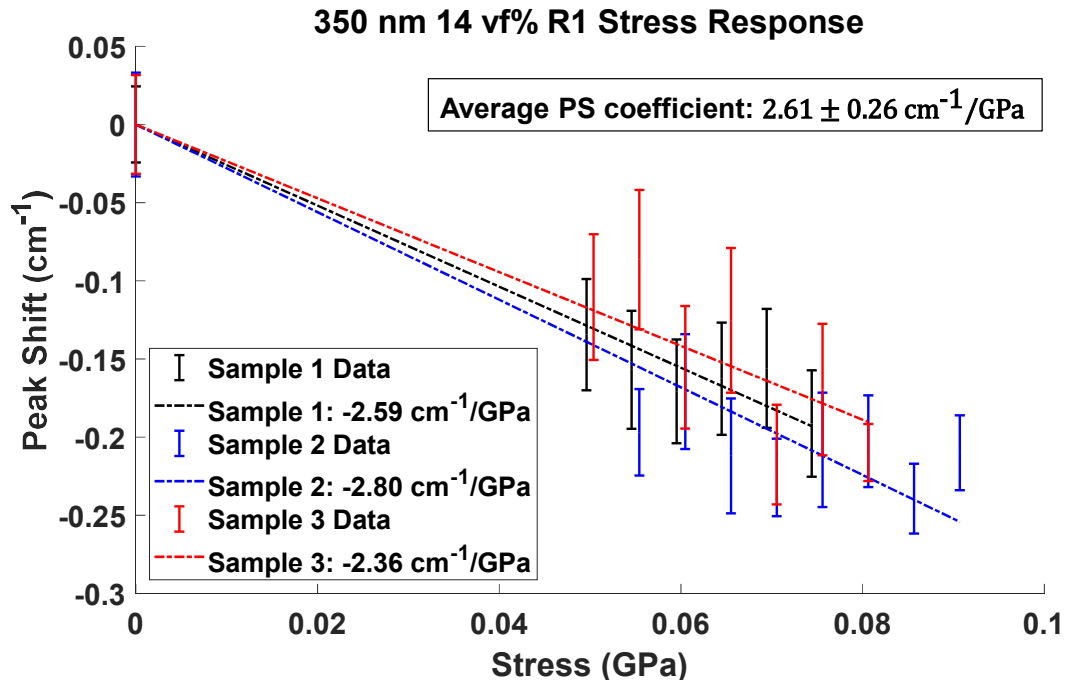


Figure 4.12: PS coefficient of 350 nm particle size and 14% VF across 3 different samples

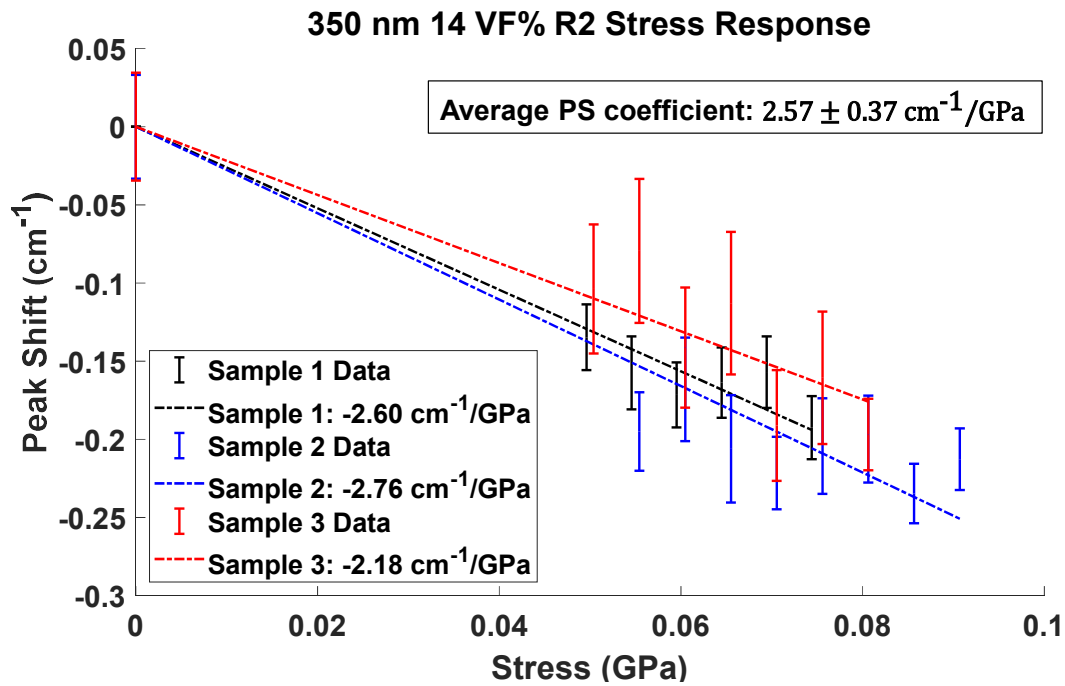


Figure 4.13: R2 PS coefficient of 350 nm particle size and 14% VF across 3 different samples.

loads as exhibited in figure 4.11. The R1 and R2 PS coefficient results indicate that the trends in each sample peakshifts are still in good agreement with each other. One reason for this could be attributed to the high SNR from this series strengthening the reliability and precision of the signal compared to the 100 and 150 nm. Another contributor may also be the better dispersion, promoting stress uniformity with the particles as seen in figure 4.1. From figures 4.12 and 4.13, the average PS coefficient for R1 and R2 are found to be 2.61 and 2.57 cm⁻¹/GPa, respectively. The R1 PS coefficient is lower than the 100 and 150 nm, while the R2 PS coefficient has a higher value.

4.4 Effect of Particle Size on Load Transfer

There is an increase of the R1 PS coefficient as the particle size decreases. The escalation of the PS coefficient indicates that greater peak shifts measured for the same applied load onto the nanocomposite. The PS coefficient has been used to represent the load transfer mechanics through a stress ratio. [1] Through this representation shown in equation 4.1, the higher PS coefficient indicates a greater load transfer applied to the particle. [1, 35]

$$\frac{\sigma_{11}}{\sigma_{applied}} = \frac{\Pi_{NC}}{\Pi_H} \quad (4.1)$$

Where Π_{NC} is the nanocomposite PS coefficient obtained through experimentation, Π_H is the hydrostatic PS coefficient for polycrystalline alumina. σ_{ii} is the stress of the particle and $\sigma_{applied}$ is the applied stress onto the composite. The relationship between the particle size and the PS coefficient has been made clear in figure 4.14, showing that as the particle size decreases the R1

PS coefficient increases. This relationship is further extended into its load transfer capabilities through the determination of the stress ratio shown in table 4.1.

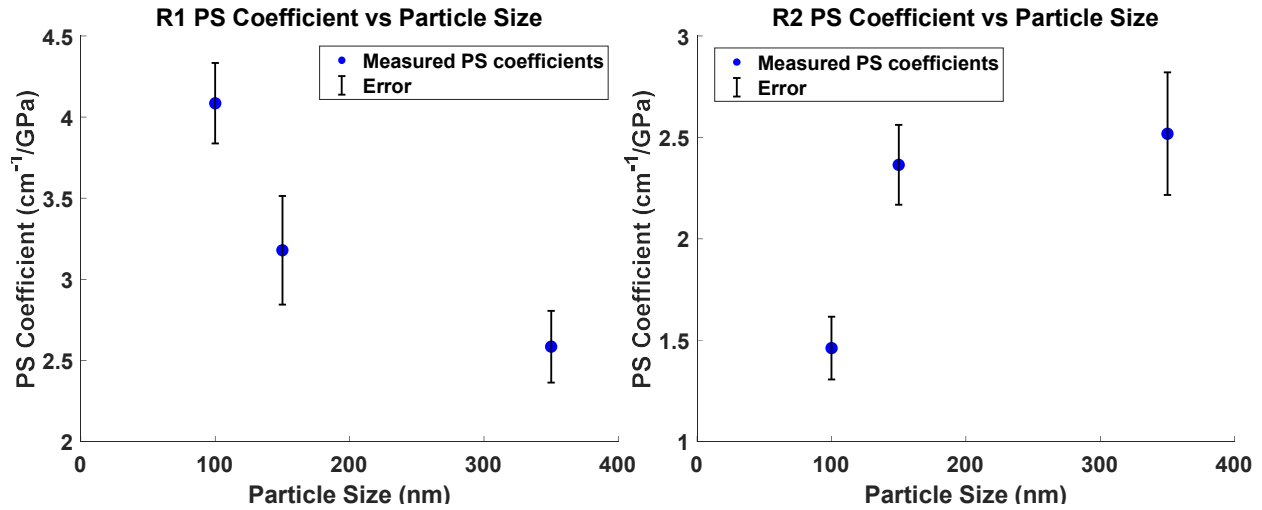


Figure 4.14: Piezo-spectroscopic coefficient vs particle size

Table 4.1: R1 and R2 PS coefficients and stress ratios, defined by equation 4.1, for particle sizes 100, 150 and 350 nm.

Particle Size	R1 PS Coefficient (cm ⁻¹ /GPa)	R2 PS Coefficient (cm ⁻¹ /GPa)	R1 Stress Ratio, $\frac{\Pi_{NC}}{\Pi_{ii}}$	R2 Stress Ratio, $\frac{\Pi_{NC}}{\Pi_{ii}}$
100 nm	4.11 ± 0.27	1.54 ± 0.15	0.54	0.19
150 nm	3.18 ± 0.33	2.41 ± 0.11	0.42	0.32
350 nm	2.61 ± 0.26	2.57 ± 0.37	0.34	0.33

The R2 PS coefficient shows to be decreasing with smaller particle sizes. This is opposite from the R1 PS coefficient trend in respects to particle size. The R-line fits were deemed acceptable across all samples and loads with a R-square value of less than 0.05 shown in table 4.2.

Table 4.2: R-square of each sample and the averages for each particle size

Sample	100 nm	150 nm	350 nm
1	0.0399 ±0.0019	0.0314 ±0.0011	0.0386 ±0.0003
2	0.0367 ±0.0025	0.0332 ±0.0021	0.0383 ±0.0003
3	0.0397 ±0.0028	0.0315 ±0.0010	0.0343 ±0.0002
Average	0.0387 ±0.0024	0.0320 ±0.0014	0.0371 ±0.0003

The fitting procedure was consistent for all data. The 100 nm R2 PS coefficient is lower than anticipated. This is possibly due to the low SNR. The effects of signal quality are likely to have affected the R2 PS coefficient measured for the 100 nm particle size. The R2 peak measurements can be improved to reflect the effects of particle size by improving the collection parameters.

The higher stress ratio for R1 indicates an increase in the load transfer in smaller particles. This can be explained by understanding the load transfer theory with the help of published literature. These higher stress ratio in the smaller particle can stem from a various factors in the composite system. Some of these variables can be assessed with Eshelbys inclusion theory. [67, 68] The classical theory dictates the total stress of the particles would be the sum strain disturbed by the filler, the mechanical strain from the applied load, and the equivalent eigenstrain. [67, 68] The first and largest contributor of additional stress originates from the specific surface area to volume ratio. [95, 140, 45] The second factor is the elevated stress concentrations due to decreased curvature. [93, 94, 95] The third aspect would be the increased percolation due to the decreased interparticle distances associated with smaller particle sizes. [141, 31, 72, 142, 27, 28] The exponential trend towards smaller particle size may indicate that 14% VF is past the percolation threshold for the 100

nm. The effects of percolation for the 350 nm is not likely to be prominent. A similar conclusion could be made for the 150 nm as the trend of Freihofer's PS coefficients has not indicated any signs percolation until 38% VF sample. [1]

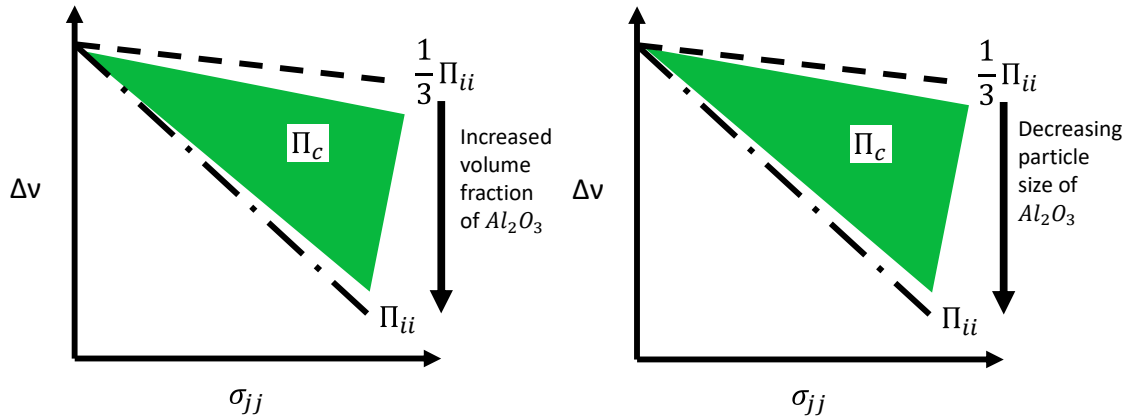


Figure 4.15: Tailoring of load transfer using particle size and volume fraction for alumina nanocomposites. The volume fraction effect on the load transfer is from Freihofer. [1]

The empirical evidence of load transfer increasing with decreasing particle size was deduced through the determination of the PS coefficient. With this, the design of alumina epoxy nanocomposites can be further tailored for maximum load transfer using both particle size and volume fraction as is portrayed in figure 4.15.

4.4.1 Luminescent Lifetime Coefficients for 14% VF with Varying Particle Sizes

In this section we will review the effects of stress in a composite system on the luminescent lifetime decay. A large variation in the lifetime decay measurements under stress was yielded in the

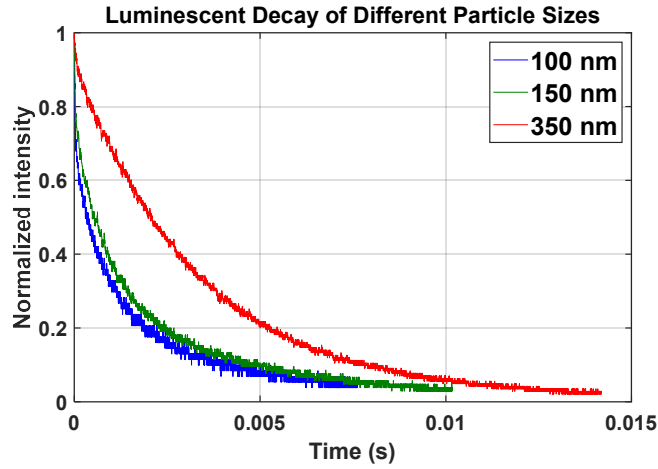


Figure 4.16: Stress free time resolved normalized luminescence of 100 nm, 150 nm, and 350 nm particle sizes

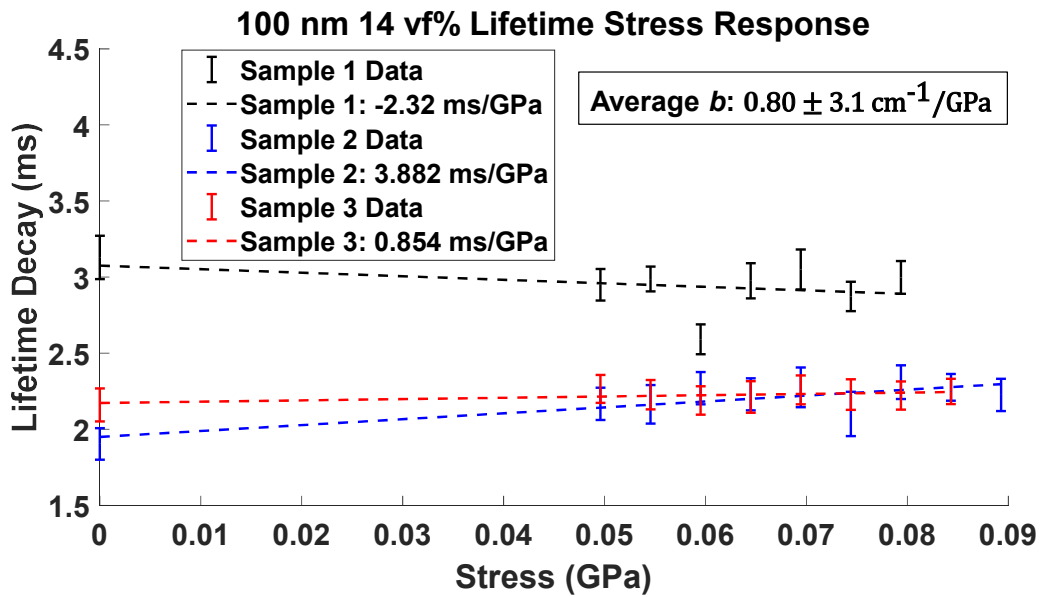


Figure 4.17: Lifetime stress sensitivity of 350 nm particle size and 14 VF%

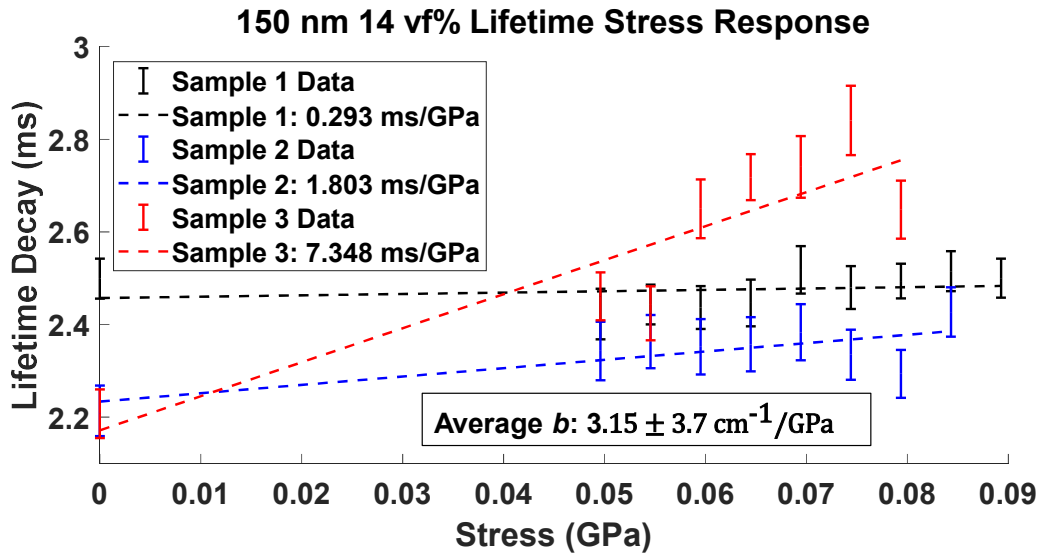


Figure 4.18: Lifetime stress sensitivity of 150 nm particle size and 14 VF%

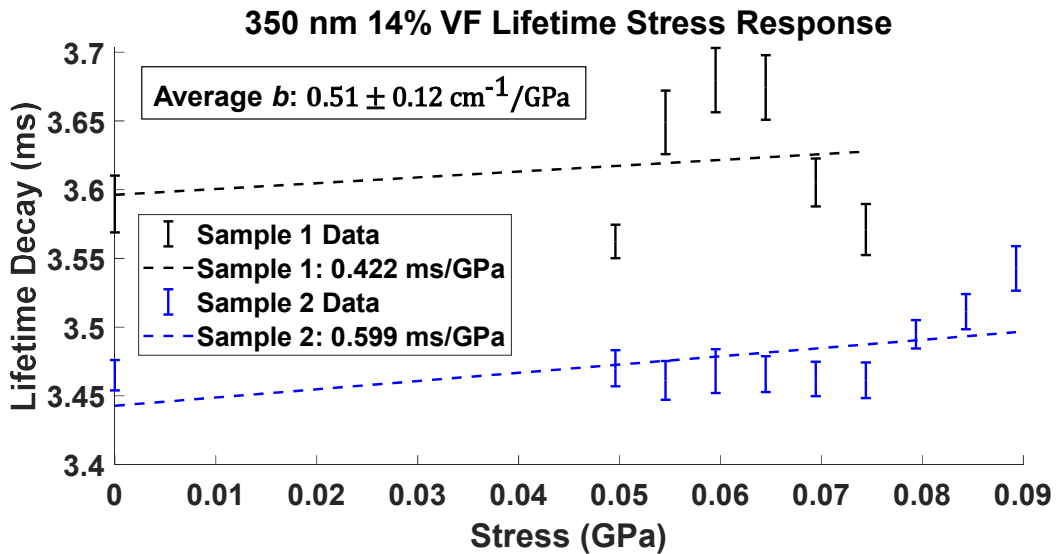


Figure 4.19: Lifetime stress sensitivity of 350 nm particle size and 14 VF%

different particle sizes. The three signals are compared in figure 4.16. The lifetime sensitivity to stress is plotted in figures 4.17, 4.18, and 4.19. During the course of the experimentation the 350 nm series was observed to have the most intense signal of the three sizes and a longer lifetime decay of 3.527. This was expected since it also had the largest SNR from the R-lines. 100 nm and 150 nm were observed to have similar luminescence and lifetime decay of 2.306 and 2.352 ms.

With the lower Cr^{3+} concentration, the 100 nm was expected to have higher lifetime decay but this did not hold true in these experiments. [143] This could first be explained with the effect of the dopant concentrations are overshadowed by the increased trap density associated with smaller particles and greater grain boundary. [122, 123, 115] The expected stretch exponential would deviate more into a bi-exponential with a fast and slow decay. [116] Secondly, the matrix may be affecting the lifetime decay as a result of the refractive index or an additional trapping effect. [144, 124, 125] Lastly, the localized agglomerations can result in a higher trap density and reduced mobility of the charge carriers and a change in the effective refractive index. [145, 146, 124] This difference could also be attributed to the variation in the particle dispersion in the surface that was optically measured and their size. It should be noted that since the lifetime was a stationary point measurement, it was unable to account for the spatial variation in the particle dispersion and the dislocation of the surface due to the applied stress.

The lifetime vs stress trends for each of the particle sizes are shown in figures 4.17, 4.18, and 4.19. From this figure, the lifetime decay coefficients at the zero load state vary to a large degree for the 100 nm series. It can be seen that b for various particle sizes often times exceeds the stress sensitive lifetime coefficient. This is seen with the 100 nm and the 150 nm series with b

Table 4.3: Lifetime stress sensitivity coefficients, $(a+\sigma b=\tau)$ and the stress ratios using the hydrostatic lifetime decay coefficient of 0.322 and 0.19 ms/GPa for low and high concentrations, respectively. [4, 5]

Particle Size	Cr ³⁺ concentration	a	b (ms/GPa)	Stress Ratio, $\frac{b_{NC}}{b_{ii}}$
100 nm	Low	2.352 ms	0.80 ±3.1	2.48
150 nm	High	2.306 ms	3.15 ±3.7	14.32
350 nm	High	3.527 ms	0.51 ±0.12	2.31

values several times larger than the bulk alumina under hydrostatic stress. The combination of a single point measurement and a varying dispersion of particles scanned may suggest that the load capacity tested was insufficient to assess the lifetime decay/stress relationship accurately. However with the 350 nm series, its values are much closer to the bulk alumina compression experiment. It could also be argued that the sensitivity or resolution of the measurements was not sufficient to accurately measuring the low intensity signal. This alone would propose that the 350 nm and the smaller particle sizes tested may not be comparable with the current scope of collection parameters.

If we were to apply the same stress ratio understanding from the frequency shift results, it would be expected that the lifetime coefficient varies with stress. The expected b for the nanocomposite, would ideally fall in between the values of 0.7 ms/GPa and 3.1 ms/GPa the uniaxial stress and hydrostatic stress coefficients, respectively. This is not the case for most of the samples as their decay rate may differ more significantly. The effects of stress on lifetime with nanoparticles in bisphenol A based matrix has not been studied extensively together. With the complex influ-

ences on charge carriers and traps and the possible effects of the matrix, this method needs to be extensively studied with this set of particles sizes and the composite structure before reliable stress measurements can be gathered.

4.4.2 DIC Results for 14% VF for Varying Particle Sizes

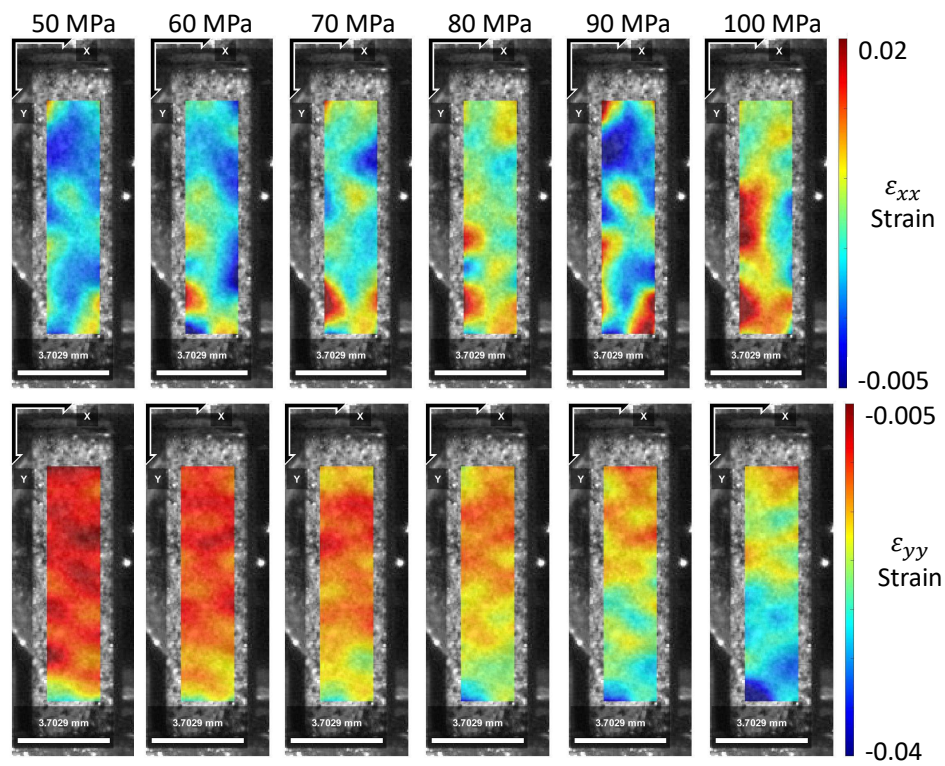


Figure 4.20: ϵ_{xx} and ϵ_{yy} maps at 10 MPa load increments of the 100 nm second sample. Non-uniaxial load becoming evident around the 100 MPa load step with the expansion of strain in the middle.

While the nano-scale load transfer mechanics of the particles has been addressed with the peak shift analysis, their effects on the fundamental material properties of the composite as a whole must be understood as well. digital image correlation is used to measure the elastic modulus and its yield strength. NCorr was used to do the post experiment DIC analysis of the back surface of the sample. [130] Here the ϵ_{xx} was used to assess if and when the material exhibited any patterns of buckling or bending during the course of the experiment as shown in figure 4.20. After confirming that no such pattern exhibited itself, the ϵ_{yy} would be averaged from the test section to assess the materials mechanical properties.

Table 4.4: Average elastic modulus of 14% VF with particle sizes of 100 nm, 150 nm, and 350 nm.

Particle Size	Volume fraction	Youngs Modulus
100 nm	14%	$35.66 \pm 9.76 \text{ GPa}$
150 nm	14%	$49.71 \pm 12.16 \text{ GPa}$
350 nm	14%	$36.79 \pm 12.03 \text{ GPa}$

The mean strains of each sample are measured and the average elastic moduli shown in table 4.4. Here it can be observed that the 150 nm series has the higher elastic modulus of all the particle sizes. It can be noted that the elastic modulus has not been significantly influenced by the differences in particle size. Using the rule of mixtures and the range of known elastic modulus for α -alumina, the effective elastic modulus of these composites is expected be in the range of 30 to 60 GPa. The 100 nm and 350 nm particle sizes identify more closely to the lower limits of the predicted range. This trend is not unexpected as previous literature has shown that particle

size does not tend to have a large effect on the material properties of the overall composite at low enough volume fractions. [47, 46, 7]

CHAPTER 5

CONCLUSION

From this work, load transfer of the nanocomposite was studied in respect to particle size. Photoluminescent piezospectroscopy was used to measure the change in load transfer. The different trials in perfecting the uniaxial compression procedure demonstrated the effects of non-uniaxial load on the alumina calibrant. Non-uniaxial loading introduced bending to the sample resulting in incorrect PS and lifetime decay stress coefficients. Uniaxial load was applied with improvements toward the experimental setup inaccuracies. With uniaxial load, the polycrystalline peakshifts and lifetime decay stress sensitivity yielded the expected values from published literature. The R1 intensity scans showed that the 350 nm series have better dispersion qualities than the smaller particle sizes. The 100 nm particle size at 14%VF were measured to have a R1 and R2 PS coefficient of 4.11 and 1.45 $\text{cm}^{-1}/\text{GPa}$, respectively. For the 150 nm particle size at 14%VF, the PS coefficients for R1 and R2 were 3.18 and 2.41 $\text{cm}^{-1}/\text{GPa}$. The average PS coefficients with the 350 nm at 14%VF for R1 and R2 are found to be 3.18 and 2.41 $\text{cm}^{-1}/\text{GPa}$, respectively. The R1 stress ratio derived from the nanocomposite and polycrystalline PS coefficients for the 100, 150 and 350 nm were 4.11, 3.18, and 2.61, respectively.

The R2 100 nm particle size PS coefficient was lower than expected and this is likely due to low SNR with high noise in the R2 region. The R2 peak measurements can be improved with

optimized collection parameters. The R1 stress ratios indicate that the load transfer increased with smaller particle sizes. The increased surface area to volume ratio, elevated stress concentrations due to decreased curvature, and increased percolation are identified to be the additional sources of increased stress in the particle. The R1 PS coefficients obtained in this study and in prior work can be used to design particle nanocomposites optimized for structural applications. The lifetime measurements stress free values showed that with the smaller particle sizes the stress free lifetime decay was shorter. This may be due to more prominent traps associated with smaller particles, the matrix, or the spatial variation of the particles. The lifetime stress sensitivity coefficients obtained could be due the lack of sensitivity and resolution in the collection parameters or the inability to account for the spatial variation unlike the peak shift results. Additional influences could be possible but further work is needed to expand the utility of lifetime measurements toward stress measurements with composite systems. The DIC measurements showed no effect of particle size in the elastic modulus with values of approximately 35, 49, and 36 GPa. These values are within the expected range from the rule of mixtures and known elastic modulus values.

LIST OF REFERENCES

- [1] G. Freihofer, A. Schülzgen, and S. Raghavan, “Multiscale mechanics to determine nanocomposite elastic properties with piezospectroscopy,” *Acta materialia*, vol. 81, pp. 211–218, 2014.
- [2] S. Raghavan, P. Imbrie, and W. A. Crossley, “Spectral analysis of r-lines and vibronic sidebands in the emission spectrum of ruby using genetic algorithms,” *Applied spectroscopy*, vol. 62, no. 7, pp. 759–765, 2008.
- [3] S. H. Margueron and D. R. Clarke, “Stress anisotropy of the r-line luminescence lifetime in single crystal cr-doped sapphire (ruby),” *Journal of applied physics*, vol. 101, no. 9, p. 093521, 2007.
- [4] L. D. Merkle, I. L. Spain, and R. C. Powell, “Effects of pressure on the spectra and lifetimes of ndxy1-xp5o14 and ruby,” *Journal of Physics C: Solid State Physics*, vol. 14, no. 14, p. 2027, 1981.
- [5] B. Jovanic, “Lifetime of the ruby r1 line under ultrahigh pressure,” *Chemical physics letters*, vol. 190, no. 5, pp. 440–442, 1992.
- [6] M. Joshi and U. Chatterjee, “Polymer nanocomposite: an advanced material for aerospace applications,” in *Advanced composite materials for aerospace engineering*. Elsevier, 2016, pp. 241–264.
- [7] J. Cho, M. Joshi, and C. Sun, “Effect of inclusion size on mechanical properties of polymeric composites with micro and nano particles,” *Composites Science and Technology*, vol. 66, no. 13, pp. 1941–1952, oct 2006.
- [8] B. Parveez, M. I. Kittur, I. A. Badruddin, S. Kamangar, M. Hussien, and M. A. Umarfarooq, “Scientific advancements in composite materials for aircraft applications: A review,” *Polymers*, vol. 14, no. 22, p. 5007, nov 2022.
- [9] S. Rana and R. Figueiro, “Advanced composites in aerospace engineering,” in *Advanced composite materials for aerospace engineering*. Elsevier, 2016, pp. 1–15.
- [10] L. Zhu, N. Li, and P. Childs, “Light-weighting in aerospace component and system design,” *Propulsion and Power Research*, vol. 7, no. 2, pp. 103–119, 2018.

- [11] S. Prashanth, K. Subbaya, K. Nithin, and S. Sachhidananda, "Fiber reinforced composites—a review," *J. Mater. Sci. Eng.*, vol. 6, no. 03, pp. 2–6, 2017.
- [12] S. Manoharan, B. Suresha, G. Ramadoss, and B. Bharath, "Effect of short fiber reinforcement on mechanical properties of hybrid phenolic composites," *J. Mater.*, vol. 2014, pp. 1–9, 2014.
- [13] I. Ibrahim, F. Mohamed, and E. Lavernia, "Particulate reinforced metal matrix composites—a review," *Journal of materials science*, vol. 26, pp. 1137–1156, 1991.
- [14] D. A. Jesson and J. F. Watts, "The interface and interphase in polymer matrix composites: effect on mechanical properties and methods for identification," *Polymer Reviews*, vol. 52, no. 3, pp. 321–354, 2012.
- [15] I. Hanhan, A. P. Selimov, D. Carolan, A. Taylor, and S. Raghavan, "Characterizing mechanical properties of hybrid alumina carbon fiber composites with piezospectroscopy," in *57th AIAA/ASCE/AHS/ASC Structures, Structural Dynamics, and Materials Conference*, 2016, p. 1413.
- [16] A. P. Selimov, R. Hoover, Q. Fouliard, A. C. Manero, P. Dackus, D. Carolan, A. Taylor, and S. Raghavan, "Characterization of hybrid carbon fiber composites using photoluminescence spectroscopy," in *58th AIAA/ASCE/AHS/ASC Structures, Structural Dynamics, and Materials Conference*, 2017, p. 0123.
- [17] S. A. Jahan, M. Abdelgader, E. Barker, J. Hernandez, R. Hoover, H. Pan, Y. Bai, D. Carolan, A. Taylor, and S. Raghavan, "Effect of functionalization on mechanical properties of hybrid carbon fiber reinforced polymer (hcfpr) composites using piezospectroscopy," in *2018 AIAA/ASCE/AHS/ASC Structures, Structural Dynamics, and Materials Conference*, 2018, p. 1378.
- [18] A. Selimov, S. A. Jahan, E. Barker, P. Dackus, D. Carolan, A. Taylor, and S. Raghavan, "Silane functionalization effects on dispersion of alumina nanoparticles in hybrid carbon fiber composites," *Applied optics*, vol. 57, no. 23, pp. 6671–6678, 2018.
- [19] A. Manero II, J. Gibson, G. Freihofer, J. Gou, and S. Raghavan, "Evaluating the effect of nano-particle additives in kevlar® 29 impact resistant composites," *Composites Science and Technology*, vol. 116, pp. 41–49, 2015.
- [20] Y. Cao, J. Sun, and D. Yu, "Preparation and properties of nano-al₂o₃ particles/polyester/epoxy resin ternary composites," *Journal of Applied Polymer Science*, vol. 83, no. 1, pp. 70–77, 2002.
- [21] F. Ke, X. Jiang, H. Xu, J. Ji, and Y. Su, "Ternary nano-caco₃/poly (ethylene terephthalate) fiber/polypropylene composites: Increased impact strength and reinforcing mechanism," *Composites Science and Technology*, vol. 72, no. 5, pp. 574–579, 2012.

- [22] D. W. Collinson, M. D. Eaton, K. R. Shull, and L. C. Brinson, "Deconvolution of stress interaction effects from atomic force spectroscopy data across polymer- particle interfaces," *Macromolecules*, vol. 52, no. 22, pp. 8940–8955, 2019.
- [23] S. Min, "Effects of volume fraction of sic particles on mechanical properties of sic/al composites," *Transactions of Nonferrous Metals Society of China*, vol. 19, no. 6, pp. 1400–1404, 2009.
- [24] S. Divagar, M. Vigneshwar, and S. Selvamani, "Impacts of nano particles on fatigue strength of aluminum based metal matrix composites for aerospace," *Materials Today: Proceedings*, vol. 3, no. 10, pp. 3734–3739, 2016.
- [25] E. A. Diler and R. Ipek, "Main and interaction effects of matrix particle size, reinforcement particle size and volume fraction on wear characteristics of al–sicp composites using central composite design," *Composites Part B: Engineering*, vol. 50, pp. 371–380, 2013.
- [26] C.-W. Nan, Y. Shen, and J. Ma, "Physical properties of composites near percolation," *Annual Review of Materials Research*, vol. 40, pp. 131–151, 2010.
- [27] S. Vionnet-Menot, C. Grimaldi, T. Maeder, S. Strässler, and P. Ryser, "Tunneling-percolation origin of nonuniversality: Theory and experiments," *Physical Review B*, vol. 71, no. 6, p. 064201, 2005.
- [28] G. Ambrosetti, C. Grimaldi, I. Balberg, T. Maeder, A. Danani, and P. Ryser, "Solution of the tunneling-percolation problem in the nanocomposite regime," *Physical Review B*, vol. 81, no. 15, p. 155434, 2010.
- [29] K. Deepa, M. Sebastian, and J. James, "Effect of interparticle distance and interfacial area on the properties of insulator-conductor composites," *Applied Physics Letters*, vol. 91, no. 20, p. 202904, 2007.
- [30] C. Sun, P. Saffari, K. Sadeghipour, and G. Baran, "Effects of particle arrangement on stress concentrations in composites," *Materials Science and Engineering: A*, vol. 405, no. 1-2, pp. 287–295, 2005.
- [31] H. Zhang, Z. Zhang, K. Friedrich, and C. Eger, "Property improvements of in situ epoxy nanocomposites with reduced interparticle distance at high nanosilica content," *Acta materialia*, vol. 54, no. 7, pp. 1833–1842, 2006.
- [32] L. Grabner, "Spectroscopic technique for the measurement of residual stress in sintered al₂o₃," *Journal of Applied Physics*, vol. 49, no. 2, pp. 580–583, feb 1978.
- [33] Q. Ma and D. R. Clarke, "Stress measurement in single-crystal and polycrystalline ceramics using their optical fluorescence," *Journal of the American Ceramic Society*, vol. 76, no. 6, pp. 1433–1440, 1993.

- [34] J. He and D. R. Clarke, "Polarization dependence of the cr^{3+} r-line fluorescence from sapphire and its application to crystal orientation and piezospectroscopic measurement," *Journal of the American Ceramic Society*, vol. 80, no. 1, pp. 69–78, 1997.
- [35] A. Stevenson, A. Jones, and S. Raghavan, "Stress-sensing nanomaterial calibrated with photostimulated luminescence emission," *Nano Letters*, vol. 11, no. 8, pp. 3274–3278, jul 2011.
- [36] G. Frehofer, A. Van Newkirk, A. Gupta, S. Seal, and S. Raghavan, "Optical stress-sensing alumina nanocomposite coatings for aerospace structures," in *55th AIAA/ASME/ASCE/AHS/SC Structures, Structural Dynamics, and Materials Conference*, 2014, p. 0159.
- [37] A. Stevenson, A. Jones, and S. Raghavan, "Real-time monitoring of an adhesive lap shear test using piezospectroscopy," in *52nd AIAA/ASME/ASCE/AHS/ASC Structures, Structural Dynamics and Materials Conference 19th AIAA/ASME/AHS Adaptive Structures Conference 13t*, 2011, p. 1814.
- [38] G. Frehofer and S. Raghavan, "Damage mapping of composites with piezospectroscopic coatings," in *56th AIAA/ASCE/AHS/ASC Structures, Structural Dynamics, and Materials Conference*, 2015, p. 1123.
- [39] R. Esteves, R. Hoover, K. Vo, S. Jahan, S. Haldar, and S. Raghavan, "Application of stress sensing coatings on metal substrates with a sub-surface notch," in *AIAA Scitech 2019 Forum*, 2019.
- [40] R. Esteves, J. Hernandez, K. Vo, R. Hoover, G. Frehofer, and S. Raghavan, "Measurements for stress sensing of composites using tailored piezospectroscopic coatings," *AIP Advances*, vol. 9, no. 5, p. 055201, 2019.
- [41] G. Frehofer, J. Dustin, H. Tat, A. Schülzgen, and S. Raghavan, "Stress and structural damage sensing piezospectroscopic coatings validated with digital image correlation," *Aip Advances*, vol. 5, no. 3, p. 037139, 2015.
- [42] D. Pinto, L. Bernardo, A. Amaro, and S. Lopes, "Mechanical properties of epoxy nanocomposites using titanium dioxide as reinforcement – a review," *Construction and Building Materials*, vol. 95, pp. 506–524, oct 2015.
- [43] R. A. Bowling, "A theoretical review of particle adhesion," *Particles on Surfaces I: Detection, Adhesion, and Removal*, pp. 129–142, 1988.
- [44] J. kang Chen, G.-T. Wang, Z.-Z. Yu, Z. Huang, and Y.-W. Mai, "Critical particle size for interfacial debonding in polymer/nanoparticle composites," *Composites Science and Technology*, vol. 70, no. 5, pp. 861–872, may 2010.

- [45] T.-T. Le, “Multiscale analysis of elastic properties of nano-reinforced materials exhibiting surface effects. application for determination of effective shear modulus,” *Journal of Composites Science*, vol. 4, no. 4, p. 172, nov 2020.
- [46] C. Verbeek, “The influence of interfacial adhesion, particle size and size distribution on the predicted mechanical properties of particulate thermoplastic composites,” *Materials Letters*, vol. 57, no. 13-14, pp. 1919–1924, 2003.
- [47] J. Spanoudakis and R. Young, “Crack propagation in a glass particle-filled epoxy resin: Part 1 effect of particle volume fraction and size,” *Journal of Materials Science*, vol. 19, pp. 473–486, 1984.
- [48] T. Gentieu, J. Jumel, A. Catapano, and J. Broughton, “Size effect in particle debonding: Comparisons between finite fracture mechanics and cohesive zone model,” *Journal of Composite Materials*, vol. 53, no. 14, pp. 1941–1954, dec 2018.
- [49] R. Singh, M. Zhang, and D. Chan, “Toughening of a brittle thermosetting polymer: effects of reinforcement particle size and volume fraction,” *Journal of materials science*, vol. 37, pp. 781–788, 2002.
- [50] J.-S. Jang, R. F. Gibson, and J. Suhr, “Characterization of particle diameter and interphase effects on young's modulus of SiO₂/epoxy particulate composites,” in *SPIE Proceedings*, N. C. Goulbourne and Z. Ounaies, Eds. SPIE, apr 2012.
- [51] K. Ghosh and S. Maiti, “Mechanical properties of silver-powder-filled polypropylene composites,” *Journal of Applied Polymer Science*, vol. 60, no. 3, pp. 323–331, 1996.
- [52] W. Xu, H. Ma, S. Ji, and H. Chen, “Analytical effective elastic properties of particulate composites with soft interfaces around anisotropic particles,” *Composites Science and Technology*, vol. 129, pp. 10–18, 2016.
- [53] J. Choi, H. Shin, S. Yang, and M. Cho, “The influence of nanoparticle size on the mechanical properties of polymer nanocomposites and the associated interphase region: A multiscale approach,” *Composite Structures*, vol. 119, pp. 365–376, 2015.
- [54] M. Paredes, C. Angammana, and S. Jayaram, “Modeling the interphase of silicone/sio₂ nanodielectrics,” in *Conference Paper*, 2015.
- [55] R. J. Young, L. Deng, T. Z. Wafy, and I. A. Kinloch, “Interfacial and internal stress transfer in carbon nanotube based nanocomposites,” *Journal of materials science*, vol. 51, pp. 344–352, 2016.
- [56] A. De la Vega, I. Kinloch, R. Young, W. Bauhofer, and K. Schulte, “Simultaneous global and local strain sensing in swent–epoxy composites by raman and impedance spectroscopy,” *Composites Science and Technology*, vol. 71, no. 2, pp. 160–166, 2011.

- [57] S. Wang, R. Liang, B. Wang, and C. Zhang, “Load-transfer in functionalized carbon nanotubes/polymer composites,” *Chemical Physics Letters*, vol. 457, no. 4-6, pp. 371–375, 2008.
- [58] R. Todd, M. Bourke, C. Borsa, and R. Brook, “Neutron diffraction measurements of residual stresses in alumina/sic nanocomposites,” *Acta materialia*, vol. 45, no. 4, pp. 1791–1800, 1997.
- [59] P. Maurya, N. Kota, J. Gibmeier, A. Wanner, and S. Roy, “Review on study of internal load transfer in metal matrix composites using diffraction techniques,” *Materials Science and Engineering: A*, p. 142973, 2022.
- [60] E. Durnberg, K. Knipe, G. Freihofer, I. Hanhan, R. Feng, and S. Raghavan, “Particle size effect on load transfer in single particle composite samples via x-ray diffraction,” in *56th AIAA/ASCE/AHS/ASC Structures, Structural Dynamics, and Materials Conference*, 2015, p. 1124.
- [61] K. Mai, E. Mäder, and M. Mühle, “Interphase characterization in composites with new non-destructive methods,” *Composites Part A: Applied Science and Manufacturing*, vol. 29, no. 9-10, pp. 1111–1119, 1998.
- [62] G. Van Assche and B. Van Mele, “Interphase formation in model composites studied by micro-thermal analysis,” *Polymer*, vol. 43, no. 17, pp. 4605–4610, 2002.
- [63] N. Sottos, R. McCullough, and W. Scott, “The influence of interphase regions on local thermal displacements in composites,” *Composites Science and Technology*, vol. 44, no. 4, pp. 319–332, 1992.
- [64] C. Tracy, “A compression test for high strength ceramics,” *Journal of testing and evaluation*, vol. 15, no. 1, pp. 14–19, 1987.
- [65] H. S. Kim, “On the rule of mixtures for the hardness of particle reinforced composites,” *Materials Science and Engineering: A*, vol. 289, no. 1-2, pp. 30–33, 2000.
- [66] G. Liu, “A step-by-step method of rule-of-mixture of fiber-and particle-reinforced composite materials,” *Composite structures*, vol. 40, no. 3-4, pp. 313–322, 1997.
- [67] J. D. Eshelby, “The force on an elastic singularity,” *Philosophical Transactions of the Royal Society of London. Series A, Mathematical and Physical Sciences*, vol. 244, no. 877, pp. 87–112, 1951.
- [68] J. Eshelby, “The determination of the elastic field of an ellipsoidal inclusion, and related problems,” *Proceedings of the royal society of London. Series A. Mathematical and physical sciences*, vol. 241, no. 1226, pp. 376–396, 1957.

- [69] H. Cox, "The elasticity and strength of paper and other fibrous materials," *British journal of applied physics*, vol. 3, no. 3, p. 72, 1952.
- [70] J. A. Nairn, "On the use of shear-lag methods for analysis of stress transfer in unidirectional composites," *Mechanics of Materials*, vol. 26, no. 2, pp. 63–80, 1997.
- [71] V. Nardone and K. Prewo, "On the strength of discontinuous silicon carbide reinforced aluminum composites," *Scripta Metallurgica*, vol. 20, no. 1, pp. 43–48, 1986.
- [72] T. Mori and K. Tanaka, "Average stress in matrix and average elastic energy of materials with misfitting inclusions," *Acta metallurgica*, vol. 21, no. 5, pp. 571–574, 1973.
- [73] A. Fedotov, "Hybrid model of homogenization of engineering elastic moduli of composites reinforced with ellipsoid particles," *Composites Part B: Engineering*, vol. 182, p. 107585, 2020.
- [74] B. Mortazavi, M. Baniassadi, J. Bardon, and S. Ahzi, "Modeling of two-phase random composite materials by finite element, mori–tanaka and strong contrast methods," *Composites Part B: Engineering*, vol. 45, no. 1, pp. 1117–1125, 2013.
- [75] J. H. Afdl and J. Kardos, "The halpin-tsai equations: a review," *Polymer Engineering & Science*, vol. 16, no. 5, pp. 344–352, 1976.
- [76] Y. Zare, "Development of halpin-tsai model for polymer nanocomposites assuming inter-phase properties and nanofiller size," *Polymer Testing*, vol. 51, pp. 69–73, 2016.
- [77] C. E. Powell and G. W. Beall, "Physical properties of polymer/clay nanocomposites," *Current Opinion in Solid State and Materials Science*, vol. 10, no. 2, pp. 73–80, 2006.
- [78] J. Zhao, D.-X. Su, J.-m. Yi, G. Cheng, L.-S. Turng, and T. Osswald, "The effect of micromechanics models on mechanical property predictions for short fiber composites," *Composite Structures*, vol. 244, p. 112229, 2020.
- [79] H. S. Kim, S. I. Hong, and S. J. Kim, "On the rule of mixtures for predicting the mechanical properties of composites with homogeneously distributed soft and hard particles," *Journal of Materials Processing Technology*, vol. 112, no. 1, pp. 109–113, 2001.
- [80] S. Ahmed and F. Jones, "A review of particulate reinforcement theories for polymer composites," *Journal of materials science*, vol. 25, pp. 4933–4942, 1990.
- [81] S. H. Foulger, "Electrical properties of composites in the vicinity of the percolation threshold," *Journal of Applied Polymer Science*, vol. 72, no. 12, pp. 1573–1582, 1999.
- [82] S. C. Baxter and C. T. Robinson, "Pseudo-percolation: Critical volume fractions and mechanical percolation in polymer nanocomposites," *Composites Science and Technology*, vol. 71, no. 10, pp. 1273–1279, 2011.

- [83] G. Zhang, Y. Xia, H. Wang, Y. Tao, G. Tao, S. Tu, and H. Wu, "A percolation model of thermal conductivity for filled polymer composites," *Journal of composite materials*, vol. 44, no. 8, pp. 963–970, 2010.
- [84] A. Fischer-Cripps, "The hertzian contact surface," *Journal of materials science*, vol. 34, no. 1, pp. 129–137, 1999.
- [85] V. Gryaznov, M. Y. Tanakov, and L. Trusov, "Plasticity and mass-transfer in contacting nanoparticles," *Journal of materials science*, vol. 27, pp. 4829–4841, 1992.
- [86] Y. Zare, K. Y. Rhee, and D. Hui, "Influences of nanoparticles aggregation/agglomeration on the interfacial/interphase and tensile properties of nanocomposites," *Composites Part B: Engineering*, vol. 122, pp. 41–46, 2017.
- [87] H. A. Rodríguez, W. M. Kriven, and H. Casanova, "Development of mechanical properties in dental resin composite: Effect of filler size and filler aggregation state," *Materials Science and Engineering: C*, vol. 101, pp. 274–282, 2019.
- [88] Y. Yan, L. Geng, and A. Li, "Experimental and numerical studies of the effect of particle size on the deformation behavior of the metal matrix composites," *Materials Science and Engineering: A*, vol. 448, no. 1-2, pp. 315–325, mar 2007.
- [89] B. Faure, G. Salazar-Alvarez, and L. Bergstrom, "Hamaker constants of iron oxide nanoparticles," *Langmuir*, vol. 27, no. 14, pp. 8659–8664, 2011.
- [90] M. P. Lutz and R. W. Zimmerman, "Effect of an inhomogeneous interphase zone on the bulk modulus and conductivity of a particulate composite," *International Journal of Solids and Structures*, vol. 42, no. 2, pp. 429–437, 2005.
- [91] K. Spanos, S. Georgantzinos, and N. Anifantis, "Mechanical properties of graphene nanocomposites: A multiscale finite element prediction," *Composite Structures*, vol. 132, pp. 536–544, 2015.
- [92] Z. Wang, Q. Lv, S. Chen, C. Li, S. Sun, and S. Hu, "Effect of interfacial bonding on interphase properties in sio2/epoxy nanocomposite: a molecular dynamics simulation study," *ACS applied materials & interfaces*, vol. 8, no. 11, pp. 7499–7508, 2016.
- [93] M. Huang and Z. Li, "Size effects on stress concentration induced by a prolate ellipsoidal particle and void nucleation mechanism," *International journal of plasticity*, vol. 21, no. 8, pp. 1568–1590, 2005.
- [94] M. Huang, "Influences of particle size and interface energy on the stress concentration induced by the oblate spheroidal particle and the void nucleation mechanism," *International journal of solids and structures*, vol. 43, no. 14-15, pp. 4097–4115, 2006.

- [95] S.-Y. Fu, X.-Q. Feng, B. Lauke, and Y.-W. Mai, “Effects of particle size, particle/matrix interface adhesion and particle loading on mechanical properties of particulate–polymer composites,” *Composites Part B: Engineering*, vol. 39, no. 6, pp. 933–961, 2008.
- [96] S. H. Margueron and D. R. Clarke, “Effect of residual stress on the luminescence lifetime of r-line emission from polycrystalline alumina formed by oxidation,” *Journal of the American Ceramic Society*, vol. 90, no. 6, pp. 1798–1801, jun 2007.
- [97] R. Christensen, D. Lipkin, D. R. Clarke, and K. Murphy, “Nondestructive evaluation of the oxidation stresses through thermal barrier coatings using cr³⁺ piezospectroscopy,” *Applied Physics Letters*, vol. 69, no. 24, pp. 3754–3756, 1996.
- [98] A. Manero II, A. Selimov, Q. Fouliard, K. Knipe, J. Wischek, C. Meid, A. M. Karlsson, M. Bartsch, and S. Raghavan, “Piezospectroscopic evaluation and damage identification for thermal barrier coatings subjected to simulated engine environments,” *Surface and Coatings Technology*, vol. 323, pp. 30–38, 2017.
- [99] G. Freihofer, D. Fugon-Dessources, E. Ergin, A. Van Newkirk, A. Gupta, S. Seal, A. Schulzgen, and S. Raghavan, “Piezospectroscopic measurements capturing the evolution of plasma spray-coating stresses with substrate loads,” *ACS applied materials & interfaces*, vol. 6, no. 3, pp. 1366–1369, 2014.
- [100] A. C. Manero, K. Knipe, C. Meid, J. Wischek, C. Lacdao, M. Smith, J. Okasinski, J. Almer, M. Bartsch, A. Karlsson *et al.*, “Comparison of thermal barrier coating stresses via high energy x-rays and piezospectroscopy,” in *53rd AIAA Aerospace Sciences Meeting*, 2015, p. 0874.
- [101] A. Wright, C. Gonzalez, A. Jones, and S. Raghavan, “Piezospectroscopic measurements on alumina-epoxy composites,” in *51st AIAA/ASME/ASCE/AHS/ASC Structures, Structural Dynamics, and Materials Conference 18th AIAA/ASME/AHS Adaptive Structures Conference 12th*, 2010, p. 2730.
- [102] A. Wright and S. Raghavan, “Effects of stress on alumina nanocomposites using piezospectroscopy,” in *Proceedings of the Society for the Advancement of Material and Process Engineering 2010 conference*, 2010.
- [103] E. E. K. L. W. G. A. S. S. R. Ashley S. Jones, Gregory Freihofer and H. Tat, “Embedded alumina nanoparticles as diagnostic coatings for structures,” in *Proceedings of the Society for the Advancement of Material and Process Engineering 2012 conference*, 2012.
- [104] R. Esteves and R. Hoover, “Piezospectroscopic coatings: Effects of alumina nanoparticle volume fraction on stress-sensing.” in *Society for the Advancement of Material and Process Engineering (SAMPE) 2018 Conference. Long Beach, Calif*, 2018.

- [105] A. Demay, J. Hernandez, P. Latorre, R. Esteves, and S. Raghavan, "Functional coatings for damage detection in aerospace structures," *Technology & Innovation*, vol. 22, no. 1, pp. 95–103, 2021.
- [106] G. Freihofer and S. Raghavan, "Characterization and performance of stress-and damage-sensing smart coatings," *Industrial Applications for Intelligent Polymers and Coatings*, pp. 91–103, 2016.
- [107] Q. Fouliard, J. Hernandez, B. Heeg, R. Ghosh, and S. Raghavan, "Phosphor thermometry instrumentation for synchronized acquisition of luminescence lifetime decay and intensity on thermal barrier coatings," *Measurement Science and Technology*, vol. 31, no. 5, p. 054007, 2020.
- [108] Q. P. Fouliard, R. Ghosh, and S. Raghavan, "Doped 8% yttria stabilized zirconia for temperature measurements on thermal barrier coatings using phosphor thermometry," in *AIAA Scitech 2020 Forum*, 2020, p. 0631.
- [109] Q. Fouliard, S. Haldar, R. Ghosh, and S. Raghavan, "Modeling luminescence behavior for phosphor thermometry applied to doped thermal barrier coating configurations," *Applied optics*, vol. 58, no. 13, pp. D68–D75, 2019.
- [110] Q. Fouliard, R. Ghosh, and S. Raghavan, "Quantifying thermal barrier coating delamination through luminescence modeling," *Surface and Coatings Technology*, vol. 399, p. 126153, 2020.
- [111] M. Maiberg, T. Hölscher, S. Zahedi-Azad, and R. Scheer, "Theoretical study of time-resolved luminescence in semiconductors. iii. trap states in the band gap," *Journal of Applied Physics*, vol. 118, no. 10, p. 105701, 2015.
- [112] G. Ju, Y. Hu, L. Chen, X. Wang, and Z. Mu, "Concentration quenching of persistent luminescence," *Physica B: Condensed Matter*, vol. 415, pp. 1–4, 2013.
- [113] D. L. Dexter and J. H. Schulman, "Theory of concentration quenching in inorganic phosphors," *The Journal of Chemical Physics*, vol. 22, no. 6, pp. 1063–1070, 1954.
- [114] N. S. Singh, R. Ningthoujam, N. Yaiphaba, S. D. Singh, and R. Vatsa, "Lifetime and quantum yield studies of dy 3+ doped gdvo 4 nanoparticles: Concentration and annealing effect," *Journal of Applied Physics*, vol. 105, no. 6, p. 064303, 2009.
- [115] B. Mutelet, P. Perriat, G. Ledoux, D. Amans, F. Lux, O. Tillement, C. Billotey, M. Janier, C. Villiers, R. Bazzi *et al.*, "Suppression of luminescence quenching at the nanometer scale in gd2o3 doped with eu3+ or tb3+: Systematic comparison between nanometric and macroscopic samples of life-time, quantum yield, radiative and non-radiative decay rates," *Journal of Applied Physics*, vol. 110, no. 9, p. 094317, 2011.

- [116] V. Pustovarov, V. Kortov, S. Zvonarev, and A. Medvedev, “Luminescent vacuum ultraviolet spectroscopy of Cr^{3+} ions in nanostructured aluminum oxide,” *Journal of luminescence*, vol. 132, no. 11, pp. 2868–2873, 2012.
- [117] C. Eckert, C. Pflitsch, and B. Atakan, “ Dy^{3+} : Al_2O_3 and (Dy^{3+} Cr^{3+}): Al_2O_3 films for temperature sensor applications derived by thermal cvd and sol-gel techniques,” *ECS Transactions*, vol. 25, no. 8, p. 1293, 2009.
- [118] S. Someya, K. Ishii, T. Munakata, and M. Saeki, “Lifetime-based measurement of stress during cyclic elastic deformation using mechanoluminescence of SrAl_2O_4 : Eu^{2+} ,” *Optics express*, vol. 22, no. 18, pp. 21991–21998, 2014.
- [119] M. R. Rahimi, G. J. Yun, G. L. Doll, and J.-S. Choi, “Effects of persistent luminescence decay on mechanoluminescence phenomena of SrAl_2O_4 : Eu^{2+} , Dy^{3+} materials,” *Optics Letters*, vol. 38, no. 20, p. 4134, oct 2013.
- [120] Y. Sato-Sorensen, “Measurements of the lifetime of the ruby r_1 line under high pressure,” *Journal of applied physics*, vol. 60, no. 8, pp. 2985–2987, 1986.
- [121] S. Sadhu, P. S. Chowdhury, and A. Patra, “Understanding the role of particle size on photophysical properties of CdS : Eu^{3+} nanocrystals,” *Journal of luminescence*, vol. 126, no. 2, pp. 387–392, 2007.
- [122] L. Xueping, F. Changyu, Z. Zhenzong, and X. Xurui, “Fluorescence decay lifetime of ultra-fine CdS and ZnS particles,” *Chinese Physics Letters*, vol. 11, no. 2, p. 127, 1994.
- [123] D. K. Williams, H. Yuan *et al.*, “Size dependence of the luminescence spectra and dynamics of Eu^{3+} : Y_2O_3 nanocrystals,” *Journal of luminescence*, vol. 83, pp. 297–300, 1999.
- [124] R. Meltzer, S. Feofilov, B. Tissue, and H. Yuan, “Dependence of fluorescence lifetimes of Y_2O_3 : Eu^{3+} nanoparticles on the surrounding medium,” *Physical Review B*, vol. 60, no. 20, p. R14012, 1999.
- [125] I. Kolesnikov, E. Golyeva, E. Borisov, E. Y. Kolesnikov, E. Lähderanta, A. Kurochkin, and M. Mikhailov, “Photoluminescence properties of Eu^{3+} -doped MgAl_2O_4 nanoparticles in various surrounding media,” *Journal of Rare Earths*, vol. 37, no. 8, pp. 806–811, 2019.
- [126] S. Raghavan and P. K. Imbrie, “Ex-situ stress measurements in polycrystalline ceramics using photo-stimulated luminescence spectroscopy and high-energy x-rays,” *Journal of the American Ceramic Society*, vol. 92, no. 7, pp. 1567–1573, 2009.
- [127] I. Hanhan, E. Durnberg, G. Freihofer, P. Akin, and S. Raghavan, “Portable piezospectroscopy system: non-contact in-situ stress sensing through high resolution photoluminescent mapping,” *Journal of Instrumentation*, vol. 9, no. 11, p. P11005, 2014.

- [128] F. Hild and S. Roux, “Digital image correlation: from displacement measurement to identification of elastic properties—a review,” *Strain*, vol. 42, no. 2, pp. 69–80, 2006.
- [129] “Standard test method for monotonic compressive strength of advanced,” American Society for Testing and Materials, Tech. Rep. Technical, 2019.
- [130] J. Blaber, B. Adair, and A. Antoniou, “Ncorr: open-source 2d digital image correlation matlab software,” *Experimental Mechanics*, vol. 55, no. 6, pp. 1105–1122, 2015.
- [131] S. T. Montgomery, S. K. Ahn, and M. Y. Lee, “Statistical analysis of compositional factors affecting the compressive strength of alumina-loaded epoxy (alox).” Sandia National Laboratories (SNL), Albuquerque, NM, and Livermore, CA . . . , Tech. Rep., 2006.
- [132] J. Millett, D. Deas, N. Bourne, and S. Montgomery, “The deviatoric response of an alumina filled epoxy composite during shock loading,” *Journal of Applied Physics*, vol. 102, no. 6, p. 063518, 2007.
- [133] R. Setchell, M. Anderson, and S. Montgomery, “Compositional effects on the shock-compression response of alumina-filled epoxy,” *Journal of applied physics*, vol. 101, no. 8, p. 083527, 2007.
- [134] B. Song, W. Chen, S. Montgomery, and M. Forrester, “Mechanical response of an alumina-filled epoxy at various strain rates,” *Journal of Composite Materials*, vol. 43, no. 14, pp. 1519–1536, 2009. [Online]. Available: <https://doi.org/10.1177/0021998308337741>
- [135] “Standard test method for compressive properties of rigid plastics,” American Society for Testing and Materials, Tech. Rep. Technical, 2016.
- [136] V. S. Romanov, S. V. Lomov, I. Verpoest, and L. Gorbatikh, “Stress magnification due to carbon nanotube agglomeration in composites,” *Composite Structures*, vol. 133, pp. 246–256, 2015.
- [137] I. Hanhan, “Hybrid carbon fiber alumina nanocomposite for non-contact stress sensing via piezospectroscopy,” Master’s thesis, University of Central Florida, 2015.
- [138] I. Hanhan, A. Selimov, D. Carolan, A. C. Taylor, and S. Raghavan, “Quantifying alumina nanoparticle dispersion in hybrid carbon fiber composites using photoluminescent spectroscopy,” *Applied Spectroscopy*, vol. 71, no. 2, pp. 258–266, 2017.
- [139] B. M. Tyson, R. K. A. Al-Rub, A. Yazdanbakhsh, and Z. Grasley, “A quantitative method for analyzing the dispersion and agglomeration of nano-particles in composite materials,” *Composites Part B: Engineering*, vol. 42, no. 6, pp. 1395–1403, sep 2011.
- [140] V. Marcadon, D. Brown, E. Hervé, P. Mélé, N. Albérola, and A. Zaoui, “Confrontation between molecular dynamics and micromechanical approaches to investigate particle size effects on the mechanical behaviour of polymer nanocomposites,” *Computational Materials Science*, vol. 79, pp. 495–505, nov 2013.

- [141] X. Deng and N. Chawla, "Modeling the effect of particle clustering on the mechanical behavior of sic particle reinforced al matrix composites," *Journal of materials science*, vol. 41, pp. 5731–5734, 2006.
- [142] P. Warren, R. Ghosh, S. Jahan, and S. Raghavan, "Investigating load transfer in ceramic reinforcements," in *Turbo Expo: Power for Land, Sea, and Air*, vol. 51128. American Society of Mechanical Engineers, 2018, p. V006T02A012.
- [143] P. M. Lewis, N. Keerthana, D. Hebbar, K. Choudhari, and S. D. Kulkarni, "Cr³⁺ doped al₂o₃ nanoparticles: Effect of cr³⁺ content in intensifying red emission," *Current Applied Physics*, vol. 32, pp. 71–77, 2021.
- [144] G. A. George, "Characterization of solid polymers by luminescence techniques," *Pure and Applied Chemistry*, vol. 57, no. 7, pp. 945–954, 1985.
- [145] S. Wang, P. Chen, S. Yu, P. Zhang, J. Li, and S. Li, "Nanoparticle dispersion and distribution in xlpe and the related dc insulation performance," *IEEE Transactions on Dielectrics and Electrical Insulation*, vol. 25, no. 6, pp. 2349–2357, 2018.
- [146] W. Wang, D. Min, and S. Li, "Understanding the conduction and breakdown properties of polyethylene nanodielectrics: effect of deep traps," *IEEE Transactions on Dielectrics and Electrical Insulation*, vol. 23, no. 1, pp. 564–572, 2016.